

OPTICAL INSTRUMENTATION USING GEOMETRIC PHASE ELEMENTS

by

Alyson Light

A thesis submitted to the faculty of  
The University of North Carolina at Charlotte  
in partial fulfillment of the requirements  
for the degree of Master of Science in  
Mechanical Engineering

Charlotte

2020

Approved by:

---

Dr. Konstantinos Falaggis

---

Dr. Rosario Porrás-Aguilar

---

Dr. Jimmie Miller

©2020  
Alyson Light  
ALL RIGHTS RESERVED

## ABSTRACT

ALYSON LIGHT. Optical instrumentation using geometric phase elements. (Under the direction of DR. KONSTANTINOS FALAGGIS)

Traditional optical instrumentation typically requires a controlled, stable environment, and this limits systems to a laboratory setting. For in-situ metrology applications and outdoor measurements, novel methods that are compact and stable are required. The focus of this thesis is to numerically evaluate, build, and test multiple interferometric holography setups to identify potential candidates for these applications. All setups used specialized geometric phase (GP) elements to perform a common-path, self-referenced measurement technique. The setups used a polarized camera sensor, consisting of a four-polarizer array of pixels, capturing high-speed measurements, otherwise known as single-shot phase shifting. The application was taken one step further, in which the complex wavefield was captured as well, which enabled digital holographic postprocessing such as numerical refocusing. In this work, the angular spectrum (AS) method was employed to refocus the wavefield numerically. Advantages of this ability are overcoming the tradeoff between depth of focus and resolution, along with diminishing the components' mechanical movement. Two different GP elements, GP lenses and GP gratings, were used to realize different shearing interferometric methods. The GP lens in the first incoherent system behaves as a concave or convex lens, based on the incoming polarization, resulting in two separate beams that interfere. All other experimental setups used incoherent and coherent light with GP gratings to spatially shear the object wavefield, enabling interference. Objects were digitally reconstructed, and parameters were evaluated to compare systems.

## ACKNOWLEDGEMENTS

I would like to sincerely show gratitude to my advisor, Dr. Konstantinos Falaggis, for his consistent dedication to the success of my projects and for teaching me about the field of optical metrology. His patience and persistence have allowed me to learn and develop skills in research and optical experimentation. His responsiveness and passion for research have allowed me to advance my knowledge and expand my opportunities for the future, and I am very grateful. I am grateful to my co-advisor, Dr. Rosario Porrás-Aguilar, for her consistent support in my projects and life. She has taught me how to set up optical experiments and enhance my presentation skills, and I am very grateful to have gained helpful knowledge from her that will carry on throughout my life. I would also like to acknowledge Dr. Jimmie Miller, for being a part of my thesis committee and for the continuous support in my projects. I would like to sincerely thank the Center for Precision Metrology at the University of North Carolina at Charlotte for the funding of my projects and support. I would like to thank Maegan Edwards for machining the components that I needed for the lab. I am thankful for my colleagues Aarush Sood, Ana Hiza Ramirez-andrade, Prithiviraj Shanmugam, Avery Turley, and Tara Newman for helping me with various tasks and difficulties throughout my projects. I would also like to acknowledge Abhinav Mishra for beginning the GP lens setup, building the preliminary experimental setup, and teaching me how it worked when I first arrived to graduate school. I would also like to acknowledge my family for the continuous support and giving me the drive to succeed.

## TABLE OF CONTENTS

LIST OF TABLES .....	viii
LIST OF FIGURES .....	ix
LIST OF ABBREVIATIONS.....	xiii
PREFACE.....	xiv
CHAPTER 1: BACKGROUND.....	1
1.1 Introduction .....	1
1.2 Brief History of Optics.....	2
1.3 Basic Properties of Light.....	3
1.3.1 Diffraction.....	3
1.3.2 Wave Theory and Propagation.....	5
1.3.3 Interference .....	7
1.4 Coherence.....	8
1.4.1 Temporal Coherence.....	8
1.4.2 Spatial Coherence .....	9
1.5 Polarization.....	10
1.6 Interferometry.....	14
1.6.1 Self-Referenced, Common-Path Interferometry .....	16
1.6.2 Phase Shifting .....	16
1.7 Non-Traditional Geometric Optics.....	17
1.7.1 Geometric Phase Lens.....	18
1.7.2 Geometric Phase Grating .....	19
1.8 Digital Holography.....	19

CHAPTER 2: EXPERIMENTAL SETUP AND PROCEDURE – GP LENS.....	21
2.1 Introduction .....	21
2.2 Experimental Setup .....	22
2.2.1 Polarized Camera Sensor .....	24
2.2.2 Image Reconstruction Distance .....	26
2.3 Numerical Refocusing.....	27
2.4 Reconstruction Results.....	29
2.5 Tested Parameters .....	31
2.6 Multi-Focus Image Fusion .....	35
2.6.1 Experimental Setup.....	36
2.6.2 Results.....	37
CHAPTER 3: EXPERIMENTAL SETUP AND PROCEDURE – GP GRATING.....	39
3.1 Introduction .....	39
3.2 Experimental Setup .....	41
3.3 Results .....	43
3.4 Comparison of GP Lens and GP Grating Experimental Setups.....	47
CHAPTER 4: COMPACT INTERFEROMETER USING COHERENT LIGHT.....	49
4.1 Introduction .....	49
4.2 Setup 1.....	49
4.2.1 Results.....	52
4.3 Setup 2.....	54
4.4 Setup 3.....	56
CHAPTER 5: CONCLUSIONS AND FUTURE WORK.....	59

REFERENCES .....	60
APPENDIX A: VARIABLES USED IN MATHEMATICAL CALCULATIONS.....	63
APPENDIX B: WIGNER ANALYSES FOR EXPERIMENTAL SETUPS .....	65

## LIST OF TABLES

TABLE A.1 List of variables used in mathematical calculations.....	63
--	----

## LIST OF FIGURES

FIGURE 1: Schematic of the thin lens approximation. ....	2
FIGURE 2: Visual representation of the diffraction of a plane wave when it exits a small opening and resulting fringe pattern. ....	4
FIGURE 3: Visual of Young's double-slit experiment and fringes obtained.....	5
FIGURE 4: Visual representation of Maxwell's discovery that light behaves as an electromagnetic wave, where $a$ represents the amplitude of the electric field, or intensity of light and $\lambda$ of the electric field, or wavelength/color of light. ....	6
FIGURE 5: Output intensity of light when two interfering waves are in phase with one another, denoted by the green dotted line. ....	7
FIGURE 6: Output intensity of light when two waves are out of phase with one another, denoted by the green dotted line. ....	8
FIGURE 7: Visual explanation of temporal coherence where $\lambda$ is the wavelength, $\Delta\lambda$ is the bandwidth, $L_c$ is temporal coherence length, and $\Delta\phi$ is the phase difference [11]. ....	9
FIGURE 8: Visual explanation of spatial coherence with source size $d$ , half angle $\theta$ , and wavelength $\lambda$ [11]. ....	9
FIGURE 9: Forms of polarization by (a) transmission, (b) reflection, and (c) scattering [13].....	11
FIGURE 10: Visualization of the different polarization states; (a) linear polarization, (b) circular polarization, (c) elliptical polarization [14]. ....	12
FIGURE 11: Schematic of Michelson interferometer design. ....	15
FIGURE 12: Schematic of how geometric phase lens behaves with different circular polarizations of light; (a) for RHCP the light will converge at a positive focal length $f_{gp}$ ; (b) LHCP will diverge at a negative focal length $-f_{gp}$ ; (c) Linearly polarized light will therefore have half diverging light and half converging [21]. ....	18
FIGURE 13: Schematic of how GP grating separates linearly polarized light into its circular components. ....	19
FIGURE 14: Schematic of GP lens system setup with (a) on-axis point source and (b) off-axis point [21]. ....	23
FIGURE 15: Experimental setup of GP lens system. ....	24

FIGURE 16: Schematic of polarized camera sensor and pixel polarization orientation. . 25

FIGURE 17: GP lens configuration and labeled distances required to calculate the reconstructed image distance;  $z_o$  is the object distance;  $z_{obj-gp}$  is the distance between the objective and GP lens;  $z_{gp-rl}$  is the distance between the GP and relay lens, or primary principal plane;  $z_h$  is the distance between the relay lens, or secondary principal plane, and the camera sensor;  $d_{gp\pm}$  is the GP lens imaging distances;  $d_{rl\pm}$  is the relay lens imaging distances from the secondary principal plane [21]..... 26

FIGURE 18: Visual representation of using the Angular Spectrum Method to numerically focus to a sharp image at distance  $z_{rec}$ . ..... 29

FIGURE 19: Experimental results with arbitrary color map after numerically refocusing to the face of a Socrates figure..... 30

FIGURE 20: (a) Reconstruction with arbitrary color map before and after numerical refocusing of a fringe pattern projected onto a viewing screen and (b) cross-section of intensity values halfway through the image. .... 30

FIGURE 21: Experimental setup to calculate the field of view; top image outlines the relay lens and the direction it was moved in green; the bottom left image is the dot target with specified dimensions; the bottom right image is the experimental setup with dot target and angled illumination. .... 32

FIGURE 22: Distance between object and objective lens ( $z_o$ ) versus FOV and the comparison of the position of the relay lens with respect to the polarized camera sensor ( $z_h$ ). ..... 33

FIGURE 23: Distance between object and the system versus effective pixel size and the comparison of the position of the relay lens with respect to the polarized camera sensor. .... 34

FIGURE 24: Reconstruction of an USAF-1951 resolution target using GP lens system with arbitrary color map. Outlined in red is the smallest group and row of distinguishable line pairs..... 35

FIGURE 25: Experimental setup of allowing the system to be exposed to multiple depths to perform multi-focus image fusion. .... 36

FIGURE 26: (a) Results of performing multi-focus image fusion with the sum of images focused at different depths (with grayscale intensity colorbar), and (b) the contrast of fringes across the 500th pixel (halfway through image)..... 37

FIGURE 27: Schematic of 4f system of GP gratings and lenses. (a) Gratings are placed at the focal length of the lenses. (b) Right grating is moved outside the focal length of the lens a distance  $\Delta x$ . (c) Right grating is moved inside the focal length of the lens a distance  $f-\Delta x$ . .... 40

FIGURE 28: Experimental GP grating setup (top) and schematic (bottom) for Fourier domain reconstruction; $f_{obj}$ is the object distance and focal length of the objective lens; $z_{CAM}$ is the distance between the second grating and camera sensor; $f$ is the focal length of the two lenses in the $4f$ system. ....	41
FIGURE 29: Pinhole experimental setup where $z_{SP}$ depicts the distance between the spotlight and pinhole and $f_{obj}$ is the distance between the pinhole and the incoherent wavefront sensor and focal length of the objective lens. ....	42
FIGURE 30: Different fringe patterns obtained when changing the position of one of the gratings in the pinhole configuration of the GP grating setup with arbitrary color map.....	43
FIGURE 31: Results of fringes at different polarizations I1-I4, amplitude with intensity color map, and phase with phase color map of complex wavefield when illuminated with incoherent light. ....	44
FIGURE 32: Results of fringes at different polarizations I1-I4, amplitude with intensity color map, and phase with phase color map of complex wavefield when illuminated with coherent light. ....	45
FIGURE 33: Results of fringes at different polarizations I1-I4, amplitude with intensity color map, and phase with phase color map of complex wavefield when illuminated with partially coherent light. ....	46
FIGURE 34: Experimental setup of USAF-1951 target (left) and reconstruction results (right). Outlined in red is the smallest group and row of distinguishable line pairs. 47	
FIGURE 35: Comparison of USAF-1951 resolution target reconstruction using GP lens setup (left and top right image) and GP grating setup (bottom right).....	48
FIGURE 36: (a) Schematic of compact interferometer: setup 1 consisting of a $4f$ configuration and (b) ray diagram. ....	50
FIGURE 37: Schematic of how wavefront propagates through setup 1 with (a) shift of positive 5 degrees (RHCP), (b) shift of negative 5 degrees (LHCP), and (c) both sheared wavefronts.....	51
FIGURE 38: Photo of experimental setup of compact interferometer setup 1.....	52
FIGURE 39: Fringe pattern results at the four different polarization angles from the polarized camera for setup 1. ....	53
FIGURE 40: Contamination of dust on mirror (left) and degree of linear polarization output from SpinView in real-time (right).....	54
FIGURE 41: Schematic of setup 2.....	55

FIGURE 42: Experimental setup of setup 2 and the resulting sheared image of a barcode sticker.....	56
FIGURE 43: (a) Schematic of single GP grating compact setup (setup 3) and (b) ray diagram. ....	57

## LIST OF ABBREVIATIONS

AS	Angular Spectrum
DoLP	Degree of Linear Polarization
FOV	Field of View
GP	Geometric Phase
GP-SIDH	Geometric Phase - Self-Interference Incoherent Digital Holography
LED	Laser-Emitting Diode
LHCP	Left-Handed Circularly Polarized Light
OPD	Optical Path Distance
RHCP	Right-Handed Circularly Polarized Light
SIDH	Self-Interference Incoherent Digital Holography
USAF	United States Air Force

## PREFACE

This thesis is the result of two consecutive mini-projects, funded by the Center for Precision Metrology at UNC Charlotte. All experimental setups use geometric phase (GP) elements to separate light and perform self-referenced common-path interferometry. Chapter 1 provides the necessary background and theory to understand how each system works. Chapter 2 explains the first project's initial setup for an interferometer system that functions using incoherent light and a GP lens to separate the beams. This setup utilizes previously implemented wave propagation algorithms to take interferometry one step further, entering the field of digital holography, where the complex wavefield is captured and numerical refocusing is possible. Experimental parameters, such as field of view, effective pixel size, and resolution are evaluated. Chapter 3 discusses the second experiment of an incoherent interferometer setup, in which a GP grating is utilized to perform spatial shearing interferometry. The resolution is evaluated for this system as well. Chapter 4 discusses the second mini-project to build a compact, handheld interferometer that works with coherent light. The goal was to be able to measure both rough and reflective or polished surfaces. Three different experimental setups were evaluated, fringe patterns were obtained, and real-time defect detection was demonstrated. Chapter 5 explains the conclusions obtained and future work to be done to further enhance discussed setups. Appendix A defines all variables used in mathematical calculations in Table A.1 and Appendix B shows the mathematical evaluations performed to numerically evaluate how the light propagates through each experimental setup.

## CHAPTER 1: BACKGROUND

### 1.1 Introduction

Optical metrology has advanced the field of precision measurement to new levels and has opened the doors to applications not possible with previous methods, due to its ability to measure very small displacements. The concept of optical metrology dates back to the invention of interferometry, which is the technique that uses the properties of light to measure surfaces. The scope of this thesis goes beyond the basic methods of interferometry in that digital holographic techniques are adopted and implemented in a laboratory setting.

Utilizing holographic techniques is a new, more sophisticated method of high-end measurement. Digital holography allows for the capturing of intensity and depth information, therefore the capability to reconstruct complex wavefields. This has attracted many fields including metrology, beam shaping, and data storage [1]. So far, holography has become a primary research field due to its ability to deliver full three-dimensional depth cue toward the viewer's eye [2].

This thesis focuses on the numerical evaluation, experimentation, and results of different optical instrumentation setups, each of which differs based on type of GP element, illumination source, and surface to be measured. Previously developed wave propagation/numerical refocusing algorithms [3], [4] were utilized throughout the experimentation, but used as a "black box," where the algorithm itself was not modified in any way during the course of this thesis.

To understand the concepts behind the experimental setups, it is important to understand the basic theories in optics, how it is used in metrology, and methods of

optical metrology as they relate to different instruments. The theory and properties of light are described in the following section to grasp the concept behind the experimental setups explained in this thesis.

## 1.2 Brief History of Optics

The understanding of optics was first sought by the Greek philosophers in tandem with the explanation of human vision [5]. In 300 B.C. to 200 A.D., Euclid and Hero were the first to discover properties of light that are still used today, including (1) the law of reflection, (2) the law of refraction and (3) that light follows the shortest path [5]. The law of reflection states when a ray of light hits a smooth surface, the angle that it hits the surface is equal to the angle it leaves the surface. The law of refraction states that light changes direction when it passes through a transparent medium.

In 1604, Kepler studied geometric optics and developed the thin lens approximation, which describes mathematically how an image is formed after going through a convex lens. This is visually represented in Figure 1.

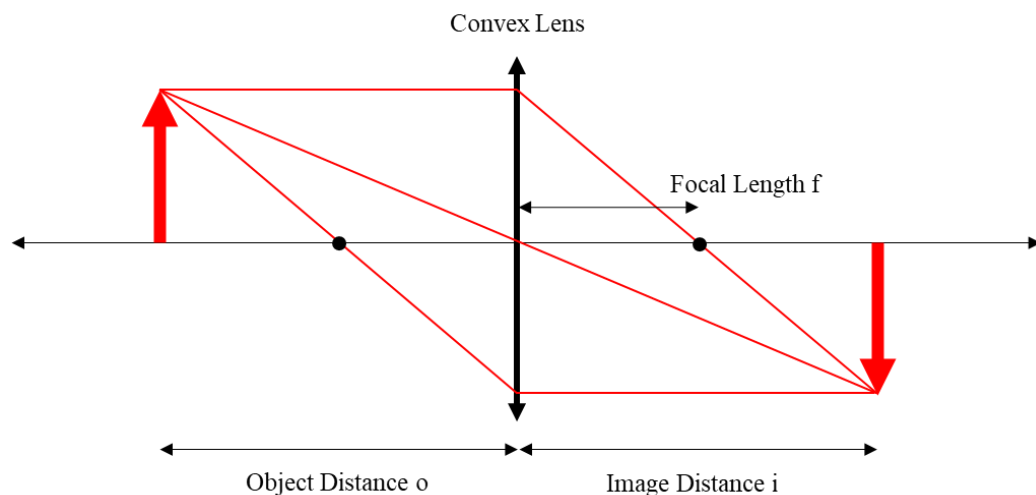


FIGURE 1: Schematic of the thin lens approximation.

As shown, the distance of the object and the focal length of the lens have a direct effect on the output image distance. The relationship is given by the thin lens Equation (1) [6]:

$$\frac{1}{o} + \frac{1}{i} = \frac{1}{f} \quad (1)$$

which formed the basis for designing optical instruments such as telescopes and microscopes, where  $o$  is the object distance,  $i$  is the image distance, and  $f$  is the focal length of the lens. The development of simple optical devices sparked the debate on the dual nature of light. In the 1600s, famous scientists such as Snell, Descartes, Fermat, Hooke, and Newton began to debate how light behaves, as a particle or as a wave.

### 1.3 Basic Properties of Light

In 1637, Descartes assumed that light consisted of tiny particles, and from this was able to form the equation for refraction [5]. Shortly after, Newton also believed that light behaved as particles through experimentation, which involved a prism illuminated with white light. From this experiment, he realized that white light consists of all colors combined and that the angle of refraction depends on the color [5]. This particle theory was criticized and later led to the wave theory of light, beginning with Grimaldi and his observance of diffraction.

#### 1.3.1 Diffraction

In 1665, Grimaldi observed through experimentation the transmission of light passing through a small hole produced patterns of bright and dark fringes, due to the interference between component rays as they pass through the small opening [7]. He gave this phenomenon the term diffraction, and therefore originated the idea that light has wave properties [7]. The theory of diffraction and resulting fringes can be visualized in Figure 2.

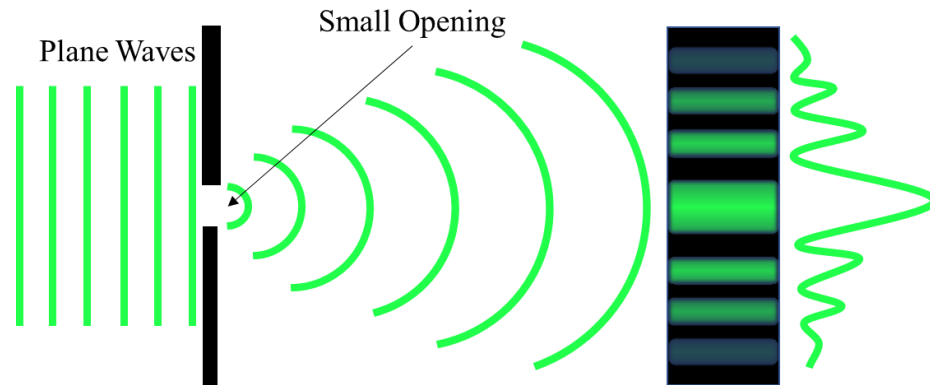


FIGURE 2: Visual representation of the diffraction of a plane wave when it exits a small opening and resulting fringe pattern.

Around 1690, the main part of the wave phenomena was explained using Huygens principle, later completed by Fresnel [8]. The principle explains that after light of constant intensity enters an opening, the wavefront is made up of the superposition of waves originating from point sources from the opening, or secondary wavelets [8]. This principle originated the foundation of geometrical optics, that light propagates in the form of spherical or planar waves [8].

Around 150 years later, Young took this concept and repeated the experiment but with two openings instead of one, ultimately concluding that these bright and dark fringes are a result of the superposition of two subfields, in his double-slit experiment, visualized in Figure 3 [8].

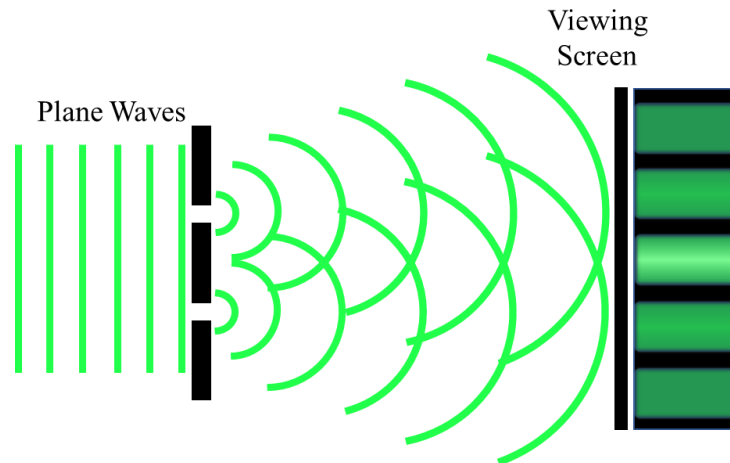


FIGURE 3: Visual of Young's double-slit experiment and fringes obtained.

Young, therefore discovered the theory of the superposition principle, which states that two waves can combine and interact with one another.

### 1.3.2 Wave Theory and Propagation

The findings of the theory of diffraction and Young's experiment led to Maxwell's discovery that light can be described as an electromagnetic wave propagating through space by moving energy and momentum [6]. This is shown in Figure 4, where the blue sinusoidal wave represents the electric field and the red represents the magnetic field. When describing a light wave and how it behaves, the electric field is typically analyzed alone, and it is known that it is paired with its magnetic field. The amplitude,  $a$ , of the electric field represents the intensity or brightness of the light. The wavelength,  $\lambda$  is the distance between two peaks of the electric field.

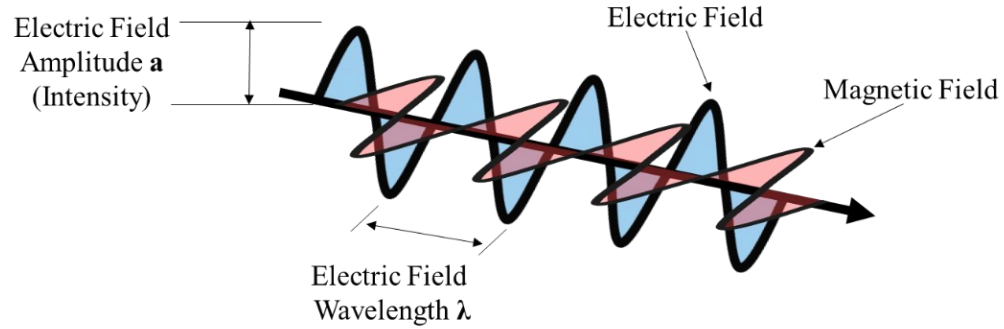


FIGURE 4: Visual representation of Maxwell's discovery that light behaves as an electromagnetic wave, where  $a$  represents the amplitude of the electric field, or intensity of light and  $\lambda$  of the electric field, or wavelength/color of light.

When considering a plane wave traveling along the  $x$ -direction, the electric field can be described mathematically with the following equation:

$$E(x, y, z, t) = a \cos(kx - \omega t + \epsilon) \quad (2)$$

where  $a$  denotes the amplitude of the electric field,  $k$  is the wave number,  $\omega$  is the temporal frequency,  $t$  is time, and  $\epsilon$  is the initial phase (described in Section 1.3.3) [9].

The electric field can be written in the form of a three-dimensional plane wave in complex notation using the following equation:

$$E(x, y, z, t) = a * e^{i(\mathbf{k} \cdot \mathbf{r} \pm \omega t + \epsilon)} \quad (3)$$

$$\mathbf{k} \cdot \mathbf{r} = k_x x + k_y y + k_z z \quad (4)$$

where  $a$  is the magnitude of the electric field,  $k$  denotes the wave number ( $k_x, k_y, k_z$ ) and  $r$  is the position vector ( $x, y, z$ ) [6]. The magnitude of  $k$  is calculated using the following equation [6]:

$$|\mathbf{k}| = \sqrt{k_x^2 + k_y^2 + k_z^2} = \frac{2\pi}{\lambda} \quad (5)$$

The superposition of multiple waves can be directly calculated using Equation (2) or (3) to construct the resulting wave equation. This phenomenon of superposition leads to interference, which is how objects can be measured using light.

### 1.3.3 Interference

Interference is a consequence of the wave nature of light, and how waves interact as a result of superposition. The final intensity from the interference of two waves is given by Equation (6) [6]:

$$I(x, y, z) = I_1 + I_2 + 2\sqrt{I_1 I_2} \cos[\Delta\Phi(x, y, z)] \quad (6)$$

Where  $I_1$  and  $I_2$  are the intensities of the individual waves and  $\Delta\Phi = \Phi_1 - \Phi_2$  is the phase difference, which is also represented in the parentheses of Equation (2) and the complex portion of Equation (3) [9]. The cosine term in the final intensity in Equation (6) produces the alternating light and dark bands in the interference pattern.

When two waves are in phase,  $\Delta\Phi = 0$ , and this produces constructive interference, as shown in Figure 5.

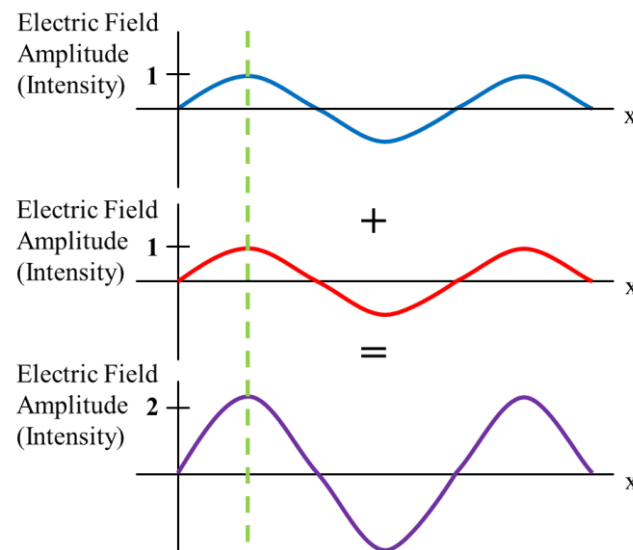


FIGURE 5: Output intensity of light when two interfering waves are in phase with one another, denoted by the green dotted line.

When two waves are out of phase,  $\Delta\Phi = \pi$ , and this produces destructive interference, as shown in is shown in Figure 6.

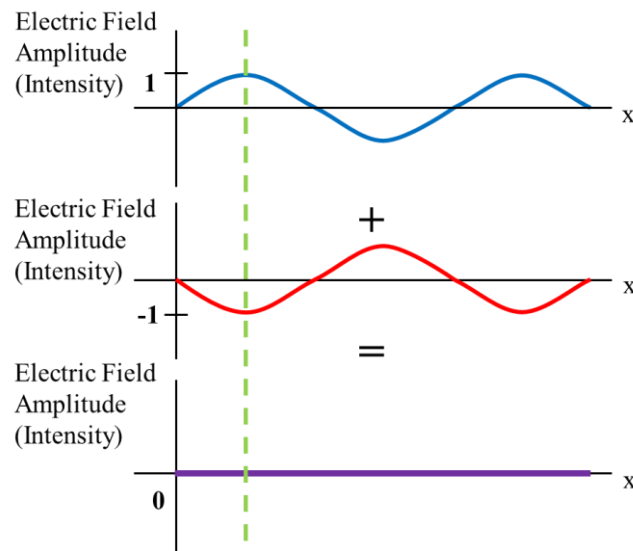


FIGURE 6: Output intensity of light when two waves are out of phase with one another, denoted by the green dotted line.

#### 1.4 Coherence

Coherence is the term used to describe the phase relationship between waves [10]. Waves that have no phase correlation and are completely independent of one another are said to be incoherent, and when there is a definite relationship, the light is labeled as coherent. There are two types of coherence, temporal and spatial coherence.

##### 1.4.1 Temporal Coherence

Temporal coherence refers to the phase of light waves at different points in time along the direction of propagation. The length of phase correlation, temporal coherence length ( $L_c$ ), is defined in terms of wavelength ( $\lambda$ ) and its bandwidth ( $\Delta\lambda$ ) using Equation (7) [11]:

$$L_c = \frac{\lambda^2}{2 \Delta\lambda} \quad (7)$$

Figure 7 visually describes temporal coherence and how its length depends on the bandwidth of wavelength.

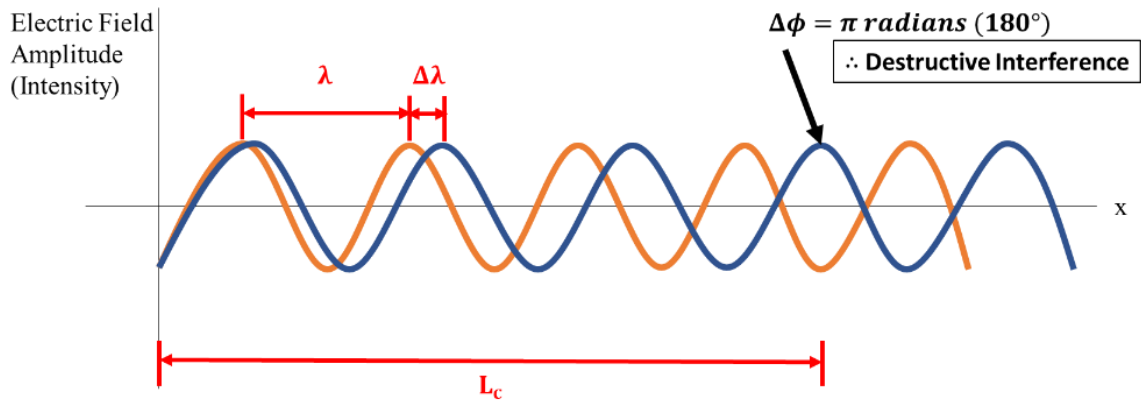


FIGURE 7: Visual explanation of temporal coherence where  $\lambda$  is the wavelength,  $\Delta\lambda$  is the bandwidth,  $L_c$  is temporal coherence length, and  $\Delta\phi$  is the phase difference [11].

Temporal coherence is higher with a smaller bandwidth of wavelength. One method of increasing coherence length is by utilizing a wavelength filter, or fluorescence bandpass filter, to only allow a certain bandwidth of wavelengths to pass through.

#### 1.4.2 Spatial Coherence

Spatially separated points in an extended light source that can interfere are spatially coherent, as shown in Figure 8 [11].

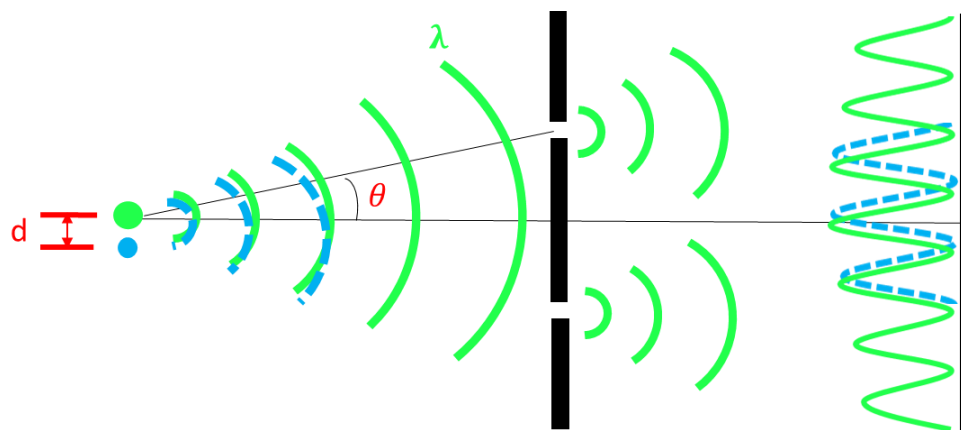


FIGURE 8: Visual explanation of spatial coherence with source size  $d$ , half angle  $\theta$ , and wavelength  $\lambda$  [11].

Therefore, this can be affected by the size of the light source [12]. Decreasing the width of the light source results in higher spatial coherence. Methods of modulating light to become spatially coherent include utilizing a spatial filter such as a pinhole or an objective lens [12]. A pinhole creates a point source with very narrow spatially separated points, therefore creates spatially coherent light. The same concept is performed by placing the object at the focal length of an objective lens, where the light is focused to a point. For all setups in this thesis, an objective lens was utilized to achieve spatial coherence.

### 1.5 Polarization

As discussed in Section 1.3.2, light is an electromagnetic wave, and the direction the electric field oscillates defines the polarization state. For example, looking at Figure 4, if one looks at the electric field as if it were approaching them, an oscillating vertical motion is seen, therefore this light is polarized vertically.

Natural and artificial light, such as light from light bulbs, typically have electric fields that vibrate in all directions perpendicular to the direction of propagation, and this form of light is defined as unpolarized. Unpolarized light can be filtered into polarized light using polarization filters. Figure 9 shows different methods of filtering and producing linear polarized states, where the red arrows indicate the direction of the resulting polarized light after passing through each filter.

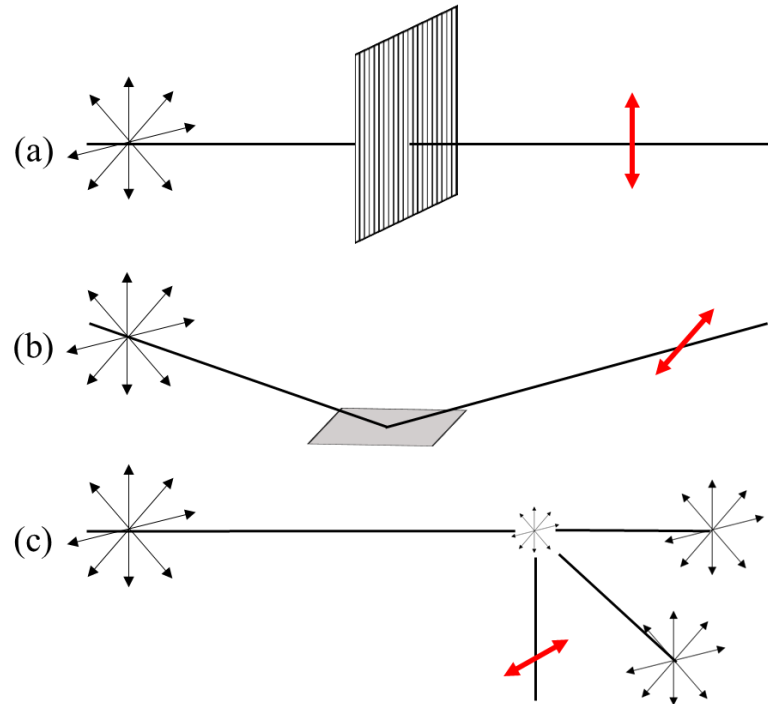


FIGURE 9: Forms of polarization by (a) transmission, (b) reflection, and (c) scattering [13].

Figure 9 (a) shows polarization through transmission, where the linear polarized filter only allows one direction of light to pass through [6], [13]. When light bounces off a reflective surface and become polarized parallel to the surface, it is polarized by means of reflection, illustrated in Figure 9 (b) [6], [13]. Another form of polarization is by scattering (see Figure 9 (c)), where linear polarized light is formed at the angle orthogonal to the incident light [13].

There are three different types of polarization based on how the electric field is oscillating, and these are linear, circular, and elliptical polarization. Linear polarization refers to light that is polarized in one plane, meaning oscillating in one direction, as shown in all examples in Figure 9 and Figure 10 (a). Circular polarization refers to two plane waves that have the same amplitude and a phase difference of 90 degrees, or  $\pi/2$

radians, as shown in Figure 10 (b). In this configuration, if one observes the wave as if it were approaching them, one sees either a clockwise or counterclockwise circular motion, perpendicular to the direction of propagation, depending on the sign of the phase shift.

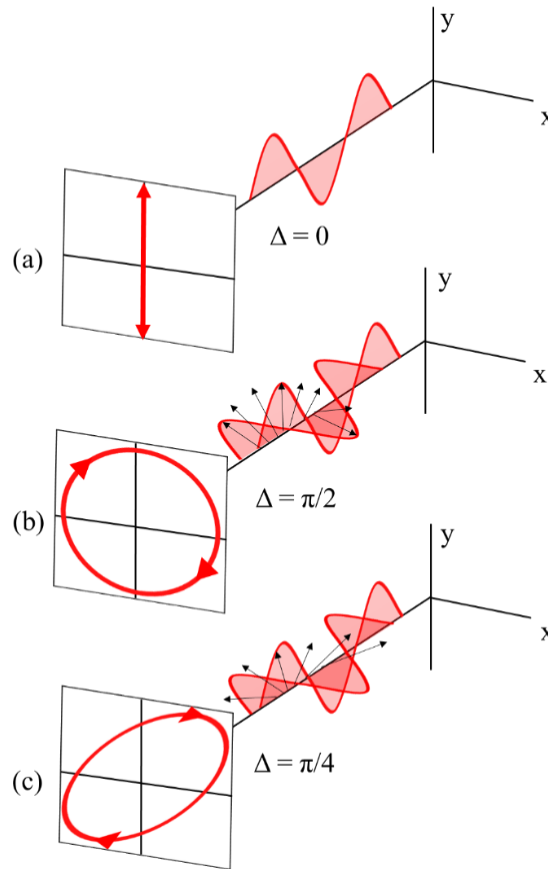


FIGURE 10: Visualization of the different polarization states; (a) linear polarization, (b) circular polarization, (c) elliptical polarization [14].

For a phase shift of  $-\pi/2$  radians ( $-90$  degrees), a counterclockwise rotation is observed, and this is called left-handed circularly polarized light (LHCP). For a phase shift of  $+\pi/2$  radians ( $+90$  degrees), the observer sees a clockwise rotation, referred to as right-handed circularly polarized light (RHCP). The third type of polarization is elliptical polarization, which can occur when either two light waves differ in amplitude and/or there is a phase

shift that is not  $\pi/2$  radians. An example of elliptical polarization is shown in Figure 10 (c), which shows the case where there is a phase shift of  $\pi/4$  radians.

Linearly polarized light can be analyzed based on its components as 50% LHCP and 50% RHCP, which can be numerically proven using Jones vectors. A Jones vector is a mathematical representation of the polarization state of a plane wave, using complex amplitudes as a column vector (see Equation (3), where  $\mathbf{k} \cdot \mathbf{r} = \text{phase angle } \phi$ ) [6]. In its normalized form, the column vector is shown as:

$$J = \frac{1}{\sqrt{a_x^2 + a_y^2}} \begin{Bmatrix} E_x = a_x e^{i\phi_x} \\ E_y = a_y e^{i\phi_y} \end{Bmatrix} \quad (8)$$

where  $E_x$  and  $E_y$  are the components of the electric field in (x, y),  $a_x$  and  $a_y$  are amplitudes in (x, y), and  $\phi_x$  and  $\phi_y$  are phase angles in (x, y) [6]. For horizontally linearly polarized light (0 degrees), the Jones vector representation of the electric field  $E_{lin}$  is:

$$E_{lin} = \begin{Bmatrix} 1 \\ 0 \end{Bmatrix} \quad (9)$$

When  $a_x = a_y$  and  $\phi_y - \phi_x = +90^\circ$ , the polarization state is RHCP, and the resulting Jones vector representation is:

$$E_{RHCP} = \frac{1}{\sqrt{2}} \begin{Bmatrix} 1 \\ +i \end{Bmatrix} \quad (10)$$

and for  $\phi_y - \phi_x = -90^\circ$ , the polarization state is LHCP, for which the Jones vector is:

$$E_{LHCP} = \frac{1}{\sqrt{2}} \begin{Bmatrix} 1 \\ -i \end{Bmatrix} \quad (11)$$

The resulting electric field from the sum of polarization states LHCP and RHCP (from Equation (10) and Equation (11)) is calculated in Equation (12):

$$E_{total} = E_{RHCP} + E_{LHCP} = \frac{1}{\sqrt{2}} \begin{Bmatrix} 1 \\ +i \end{Bmatrix} + \frac{1}{\sqrt{2}} \begin{Bmatrix} 1 \\ -i \end{Bmatrix} = \sqrt{2} \begin{Bmatrix} 1 \\ 0 \end{Bmatrix} \quad (12)$$

Equation (12) has a result of horizontally polarized light (see Equation (9)) with a normalizing factor. Therefore, it is accurate to state that linear polarized light can be analyzed as half RHCP and half LHCP. The GP lens and GP grating utilized in the interferometric setups of this thesis use this property to shear the input wavefield to perform interferometry.

### 1.6 Interferometry

Interferometry utilizes the wave behavior of light to measure object surfaces in a technique that splits a wavefront and superimposes them to interfere. Typically, one wavefront is directed to the object, known as the object wave, and the other to a reference surface, the reference wave. The waves travel different optical path distances (OPD) when the object wave observes different angles or shapes of the object surface, and the phase difference between the object wave and reference wave characterizes the surface that is being measured. The interference pattern that is formed as a result of the phase difference gives the phase information of the object. This technique is utilized in many fields, including optical metrology, holography, astronomy, fiber optics, etc. One important benefit of interferometry is that it is a technique that can measure very small variations on a surface. A major advantage of using interferometry for measurement over other methods is that it does not require mechanical contact with the object surface. Therefore there is generally no risk of damage.

In conventional interferometer designs such as in a Michelson interferometer setup, the light source is split into two beams by a beamsplitter. After the beams are split into their separate paths, one beam hits the object, and the other beam hits a reference

mirror. The light beams then bounce back and recombine onto the sensor, detector, or viewing screen. This configuration is visually represented in Figure 11.

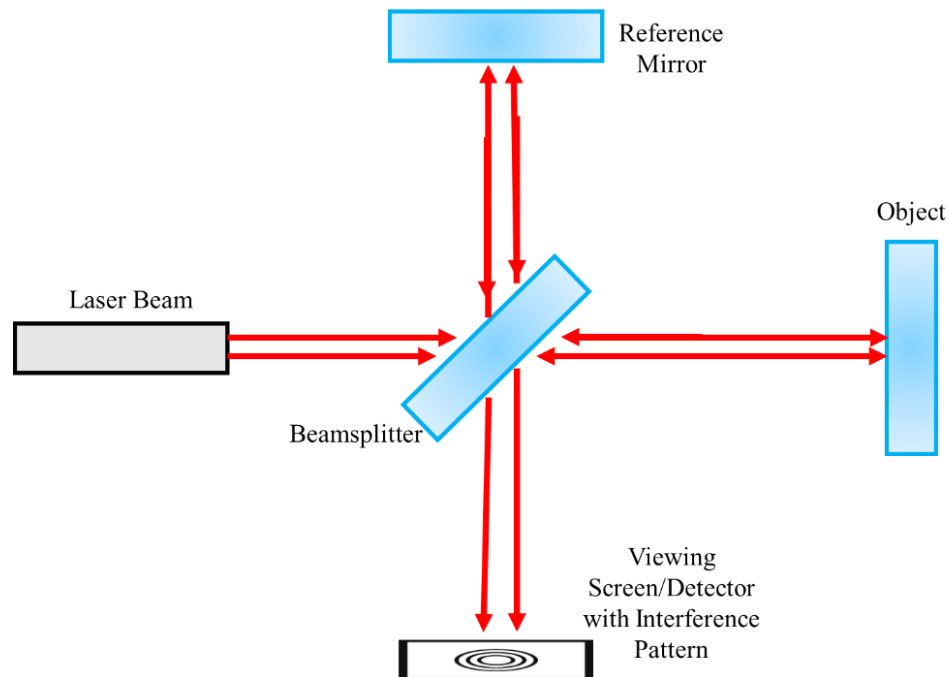


FIGURE 11: Schematic of Michelson interferometer design.

Moving the reference mirror by a known distance changes the OPD between the two waves and hence affects the interference pattern at the detector due to the shift in phase. Using known amounts of phase shifts, three-dimensional surfaces can be measured using phase shifting techniques (see further detail in Section 1.6.2.). There are several types of interferometers, and they vary based on the method of interference, the type of surface it is meant to measure, the components utilized, the type of light source used, etc. However, all interferometers use a similar principle using interference of light waves. This thesis uses a self-referenced common-path shearing interferometry technique.

### 1.6.1 Self-Referenced, Common-Path Interferometry

As opposed to conventional interferometer designs, where the beam is split into an object wave and reference wave that travel separate paths, a common-path interferometer is a system in which both beams that interfere travel the same path [15]. Due to the common path configuration, both wavefronts typically experience the same external influences that nullify each other. Therefore, unlike setups such as the Michelson, external influences can be compensated using common-path systems, giving them more robustness; thus making them more suitable for applications such as in-situ metrology in manufacturing and metrology in harsh environments. The term “self-referenced” is a method of interferometry in which the reference wave is a copy of the object wave, shifted or modified in some small manner, which diminishes the need for a well-known reference mirror. A common type of interferometry that uses both the common path and self-referenced techniques is shearing interferometry, where two copies of the object wave are spatially separated by a small distance [16]. All experimental setups in this thesis are common-path and self-referenced.

### 1.6.2 Phase Shifting

Phase shifting interferometry is one of the most powerful tools in measuring phase of an object surface [17]. The idea refers to taking three or more measurements of the intensity distribution, with each measurement stepping the phase difference of the interfering beams in some known manner [18]. From these measurements, it is possible to determine the phase distribution, which has been proven to allow for high precision measurements in surface characterization and capturing three-dimensional information of the object surface. One method of shifting the phase can be performed by mechanical

movement using a piezoelectric transducer. Figure 11 shows an example of this method using a Michelson interferometer setup, where phase shifting is performed by moving the reference mirror with known step sizes. Phase shifting can be performed by using three steps to as many as twenty, and the algorithms used to solve for the phase vary because there is a wide range of mathematical methods of doing so [19]. There are several advantages to phase shifting, including fast measurement speed, high phase-measurement accuracy, etc. [18].

In this thesis, a method called single-shot phase shifting was utilized to measure the phase without mechanically moving components and without any time delay caused by the phase shifting process. This was performed by using a polarization camera containing four different polarizations, therefore different intensities, in a pixel array format to capture four different phase shifts at once. The four shifted intensity maps are typically used to calculate phase  $\phi$  in standard interferometry [6]:

$$\phi(x, y) = \tan^{-1} \left( \frac{I_4(x, y) - I_2(x, y)}{I_3(x, y) - I_1(x, y)} \right) \quad (13)$$

where  $I_1$  through  $I_4$  are the intensities at 0, 45, 90, and 135 degrees of polarization.

Additional details for the camera sensor and methods used in this thesis are explained in chapter 2 (see Section 2.2.1).

### 1.7 Non-Traditional Geometric Optics

Polarization-sensitive optical components were utilized in the experimental setups presented in this thesis. As a result of the advances in the fields of optics and manufacturing, light can be manipulated based on its polarization in new and compact ways when developing optical interferometer systems.

### 1.7.1 Geometric Phase Lens

A polarization-directed flat lens, or geometric phase (GP) lens, was utilized in the first experimental setup, and has dimensions of 25 x 25 x 0.45 mm, making it ideal for compact optical systems [20]. It is composed of polymerized liquid crystal thin-films that behave differently for the different circular polarizations of light [21]. If the incoming light is strictly RHCP or LHCP, once it reaches the GP lens, the RHCP will converge and LHCP will diverge, as shown in Figure 12 (a) and (b).

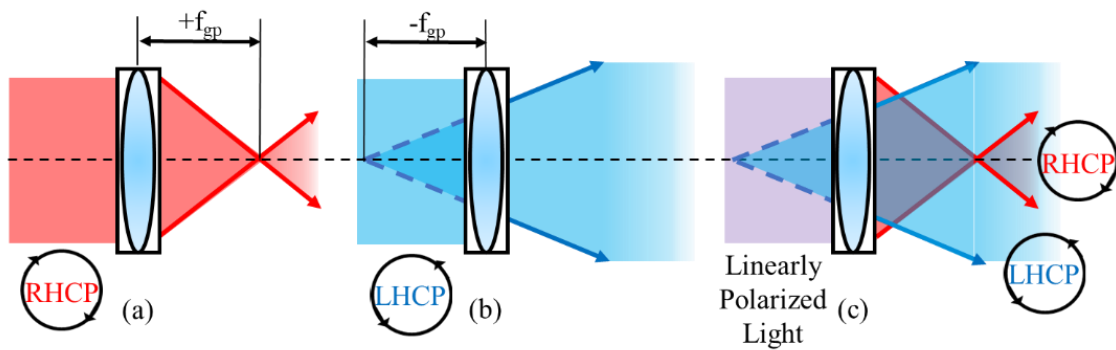


FIGURE 12: Schematic of how geometric phase lens behaves with different circular polarizations of light; (a) for RHCP the light will converge at a positive focal length  $f_{gp}$ ; (b) LHCP will diverge at a negative focal length  $-f_{gp}$ ; (c) Linearly polarized light will therefore have half diverging light and half converging [21].

In the case the incoming light is linearly polarized, which will be the case for every setup in this thesis, half of the light will diverge, and half the light will converge. This is a consequence of the fact that linearly polarized light is made of 50% RHCP and 50% LHCP (see Equation (12)). As a result, the two output waves will be circularly polarized as shown in Figure 12 (c). An example of single-shot phase measurements using GP lenses is given in [20].

### 1.7.2 Geometric Phase Grating

Another optical component utilized in experimental setups is called a diffraction polarization grating, or geometric phase (GP) grating. This component, similar to the GP lens, is sensitive to the polarization state of the incoming light. The GP grating is the same size as the GP lens; therefore, it is compact and lightweight. The GP grating is designed for high transmission rates at greater than 96% diffraction efficiency, with a maximum of 4% leakage for a wavelength range of 450-650 nm (according to Edmund Optics specifications).

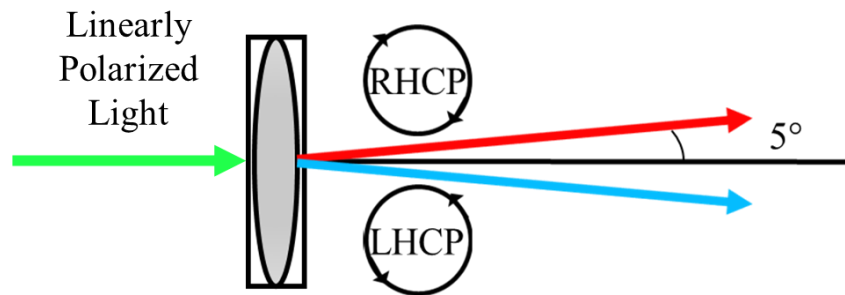


FIGURE 13: Schematic of how GP grating separates linearly polarized light into its circular components.

As with the GP lens, for incoming linearly polarized light, half the light will diffract at a positive 5 degrees and the other half at negative 5 degrees, as shown in Figure 13. For the sake of clarification, if strictly RHCP was entering the GP grating, all of the light would diffract at an angle of positive 5 degrees. The positional displacement of the wavefronts have the ability to interfere with each other, performing shearing interferometry.

### 1.8 Digital Holography

The concept of holography was first invented by Dennis Gabor in 1947 while attempting to improve the resolution of electron microscopes, and has been described as the greatest imaging technique due to its ability to capture a complete three-dimensional

volume from a single image or to perform numerical refocusing [22], [23]. Essentially, holography is a technique that applies the principles of interferometry and takes it one step further. Interferometry captures only the phase, whereas holography captures the complex wavefield from the object surface and thereby simultaneously recording both intensity and phase information. The phase is measured by recording an interference pattern from the measured object and a reference wave, and this interference result is what is known as a hologram, similar to interferometry [23].

Interference requires high light intensity, high stability in the optical setup, and a relatively narrow bandwidth light source and so it is usually necessary to have coherent light when creating holograms [24]. Therefore, holography has not been widely used in settings that image using natural light such as microscopes, telescopes, etc. [21], [23], [25]. However, the requirement of coherence has been challenged and there has been great interest in manipulating incoherent light to perform holographic interferometry.

The freedom to reconstruct holograms using incoherent light opens up numerous applications including outdoor measurements, astronomy, microscopy, etc. [24]. A common method of incoherent holography is using the property that each point on an incoherently illuminated object acts as a point source that is self-spatially coherent and can interfere with a spatially shifted copy of itself [24]. Using this property is known as a self-referencing technique (see Section 1.6.1), and systems that utilize this to reconstruct holograms digitally are classified as self-interference incoherent digital holography, or SIDH [21]. Chapter 2 and 3 of this thesis are SIDH systems.

## CHAPTER 2: EXPERIMENTAL SETUP AND PROCEDURE – GP LENS

### 2.1 Introduction

The first project involved developing an interferometer system that utilized incoherent light, eliminating the need for an expensive coherent light source, reducing the overall cost of the system. An additional goal for this system was the ability to perform numerical refocusing, which was achieved using a digital holographic technique of capturing the complex wavefield and a previously developed wave propagation algorithm [3], [4]. This GP lens setup was termed a GP-SIDH (Geometric Phase - Self-Interference Incoherent Digital Holography) system [21], due to the utilization of a GP lens to separate the light into two beams originating from the same source.

For interference to occur using incoherent light, it is typically necessary for the object to be placed in the Fourier plane, or at the focal length of an objective lens, which is the plane where the rays converge to a point. When in the Fourier plane, incoherent light is scattered off the object and each point on the object acts as a point source producing spherical wavefronts. The objective lens will collect these wavefronts and convert them to plane waves, obtaining spatial coherence, therefore enabling interference [21]. The proposed method captured the complex wavefield using a polarized camera sensor (further detail in Section 2.2.1), and numerical refocusing was performed to reconstruct in-focus holograms. Parameters of the system were evaluated such as resolution, field of view, and effective pixel size.

The wave propagation/numerical refocusing algorithm allowed the implementation of capturing multiple depths to perform multi-focus image fusion, using another previously developed image fusion algorithm [26], [27]. An artificial image that

has multiple depths in focus was digitally reconstructed without the drawback of reducing resolution with an increased depth of focus.

## 2.2 Experimental Setup

The basic principle of the GP lens system was based on two concepts. The first was using an objective lens in front of the system to transform the incoming incoherent light scattered off the object to be spatially coherent. Spatial coherence was obtained; therefore interference was achievable. The second concept was to guide the light through a GP lens, which, as previously stated, behaves as a concave and convex lens based on the different circular polarizations of light. The two beams were separated, the wavefronts were reimaged and flattened by a relay lens, and the waves interfered at the polarized camera sensor; therefore an interferometer was formed.

The linear polarizer was placed after the objective lens so only 0-degree linearly polarized light entered the system, therefore when the light reached the GP lens, it would be perfectly separated in half (see Equation (12)). A fluorescence bandpass filter filtered the wavelength so that only green light would enter the system, thus temporal coherence was raised. These principles are represented visually in Figure 14, noting that the wavefronts shown after the GP lens are both the same wavelength, but one is colored blue for visualization purposes. Figure 14 (a) shows how the on-axis point source from the object propagates through the system, and Figure 14 (b) shows how an off-axis point propagates. As shown in Figure 14 (b), the light after the objective lens becomes spatially coherent, but the plane waves travel at an angle, which corresponds to a shift in the output to the camera sensor.

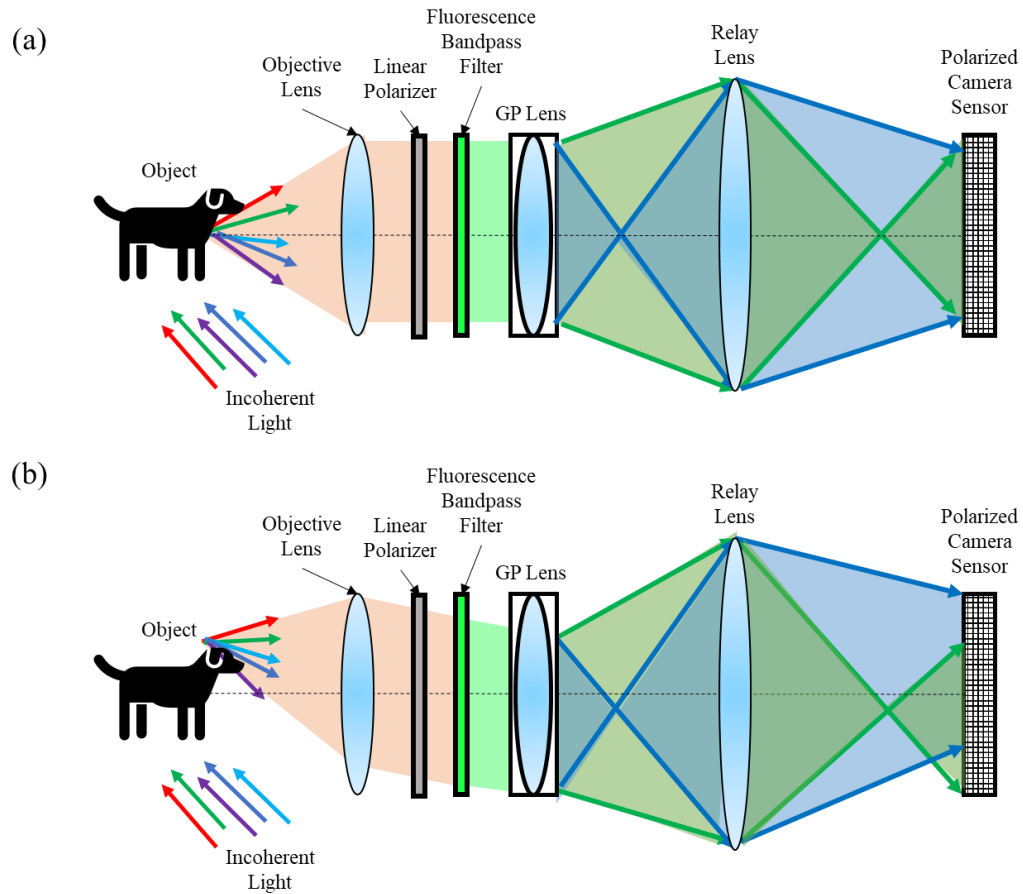


FIGURE 14: Schematic of GP lens system setup with (a) on-axis point source and (b) off-axis point [21].

The GP lens system was inspired by a publication by Choi with minor adjustments such as method of phase shifting [21].

The experimental setup and labeled components are shown in Figure 15, which is inverted and identical to the schematic in Figure 14. The system consisted of an objective lens, which has a focal length of 100 mm, a linear polarizer, followed by a fluorescence bandpass filter with a center wavelength of 520 nm, a bandwidth of 10 nm, and 93% transmission efficiency. After the fluorescence bandpass filter is the GP lens, and a relay lens to reimage, adjust the magnification, and flatten the wavefronts to the camera sensor [21]. Lastly, there was a polarized camera sensor to capture the wavefronts.

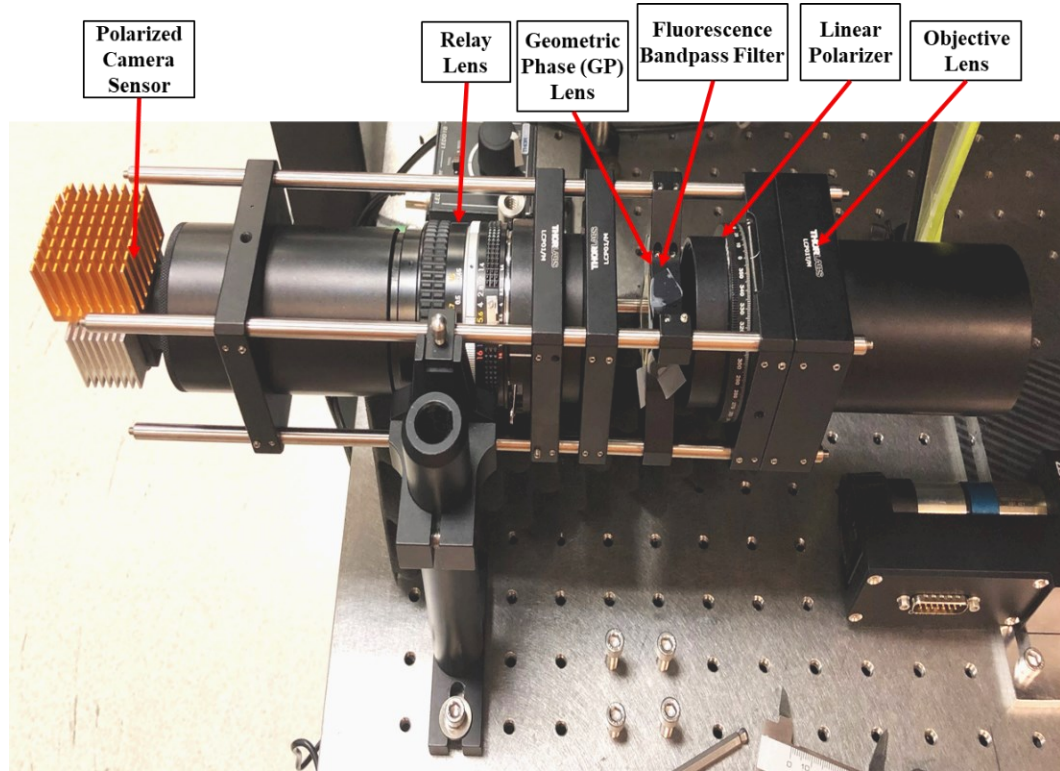


FIGURE 15: Experimental setup of GP lens system.

### 2.2.1 Polarized Camera Sensor

The GP lens setup (and all setups in this thesis) used the Flir Blackfly S, which is a monochromatic, polarized camera sensor. This camera sensor consists of a four-polarizer array of pixels at angles of 0, 45, 90, and 135 degrees, which results in four different intensities and phase shifts at different angles (see Section 1.6.2 for phase shifting explanation). A section of the camera sensor and pixel orientation can be visualized in Figure 16. Once the circularly polarized wavefronts from the GP lens reach the sensor, at each angle of polarization of pixels, the polarization state will change, acting as a linear polarizer at each angle.

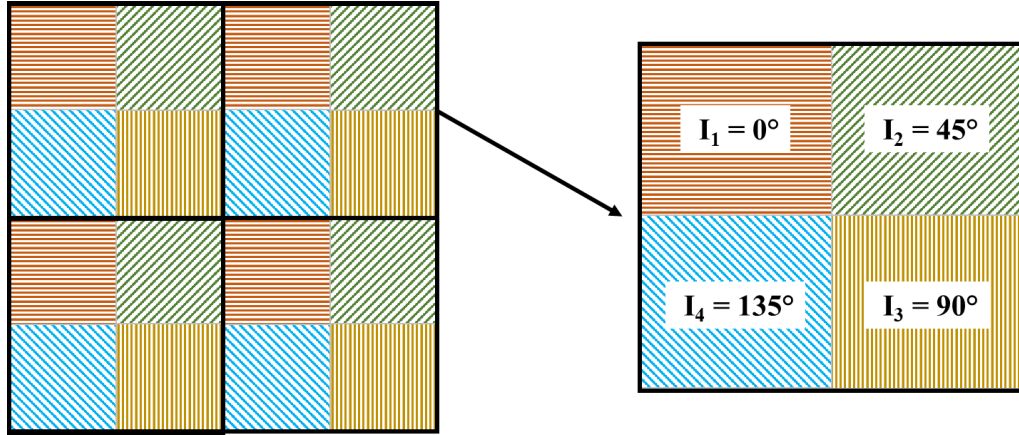


FIGURE 16: Schematic of polarized camera sensor and pixel polarization orientation.

The polarizers on the pixels at angle  $\Omega$  can be mathematically represented using Jones vector  $J_P$  [6], [21]:

$$J_P(\Omega) = \begin{bmatrix} \cos^2 \Omega & \cos \Omega \sin \Omega \\ \cos \Omega \sin \Omega & \sin^2 \Omega \end{bmatrix} \quad (14)$$

Therefore, when RHCP and LHCP reach the polarized sensor (see Equation (10) and (11)), the mathematical output polarization  $E'$  is:

$$E' = \begin{bmatrix} \cos^2 \Omega & \cos \Omega \sin \Omega \\ \cos \Omega \sin \Omega & \sin^2 \Omega \end{bmatrix} \left( \begin{Bmatrix} 1 \\ +i \end{Bmatrix} e^{i\phi} + \begin{Bmatrix} 1 \\ -i \end{Bmatrix} e^{i\phi} \right) = \cos(\Omega + \phi) \begin{bmatrix} \cos \Omega \\ \sin \Omega \end{bmatrix} \quad (15)$$

where  $\phi$  represents the phase modulation due to the GP lens [21].

In standard interferometry, the polarized camera sensor is used to perform single-shot phase shifting (see Section 1.4.3) using the shifted intensities  $I_1$  through  $I_4$  to calculate the phase  $\phi$  (see Equation (13)). For this thesis, the concept utilized was digital holography, where the complex wavefield  $U_H$  was captured using the intensities  $I_k$  of the four different  $k$  polarizations from the polarized camera sensor which were calculated by:

$$I_k = A + B e^{i(2\Omega + 2\phi)} \quad (16)$$

from the Jones equations, where  $A$  is the sum of intensities,  $B$  is the square root of the product of intensities, and  $\Omega$  is the polarization angle set by the camera pixel (0, 45, 90,

and 135 degrees), therefore a four-step phase shifting method with a 90 degree phase step was performed [21].  $\Phi$  again is the phase modulation results from the GP lens. The complex wavefield was calculated with the following [21]:

$$U_H = (I_4 - I_2) - i(I_3 - I_1) \quad (17)$$

Equation (17) allows for the capturing of both amplitude and phase information, which gives the ability to numerically refocus to any desired depth when inputted into a previously developed wave propagation/numerical refocusing algorithm that uses the classical angular spectrum method (see Section 2.3) [3], [4].

### 2.2.2 Image Reconstruction Distance

The wave propagation code requires an input of the distance where the sharp image is formed. The parameters required to calculate this distance are shown in Figure 17 and labeled in the description.

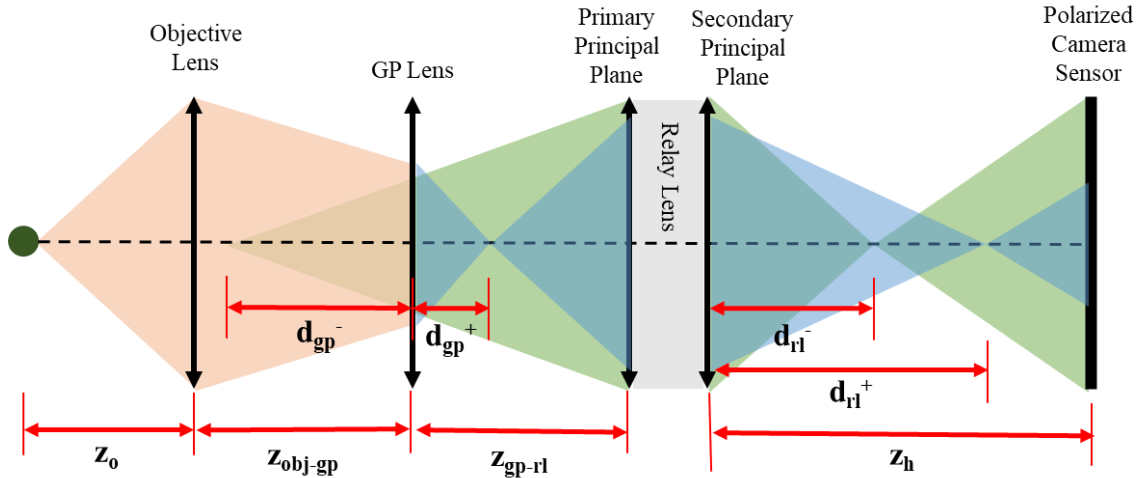


FIGURE 17: GP lens configuration and labeled distances required to calculate the reconstructed image distance;  $z_0$  is the object distance;  $z_{\text{obj-gp}}$  is the distance between the objective and GP lens;  $z_{\text{gp-rl}}$  is the distance between the GP and relay lens, or primary principal plane;  $z_h$  is the distance between the relay lens, or secondary principal plane, and the camera sensor;  $d_{\text{gp}\pm}$  is the GP lens imaging distances;  $d_{\text{rl}\pm}$  is the relay lens imaging distances from the secondary principal plane [21].

The reconstruction distance was calculated from the following equations derived from Choi [21]. First, the imaging distance from the objective and GP lens was calculated using Equation (18) from both the GP lenses positive and negative focal lengths [21]:

$$d_{gp}^{\pm} = \frac{\pm z_{obj-gp} f_{gp} (z_o - f_o) \mp f_o f_{gp} z_o}{(z_{obj-gp} \mp f_{gp})(z_o - f_o) - f_o z_o} \quad (18)$$

Next, the distances after the relay lens were calculated [21]:

$$d_{rl}^{\pm} = \frac{f_{rl}(z_{gp-rl} - d_{gp}^{\mp})}{z_{gp-rl} - d_{gp}^{\pm} - f_{rl}} \quad (19)$$

Then, the reconstruction distance of the final image was calculated with Equation (19) in the following equation [21]:

$$z_{rec}^{\pm} = \frac{(z_h - d_{rl}^{\mp})(d_{rl}^{\pm} - z_h)}{\pm \Delta d_{rl}} \quad (20)$$

Using Equation (20) the sharp image distance was known for this system, and this distance was inputted into the wave propagation/numerical refocusing algorithm for every measurement to reconstruct in-focus holograms [3], [4].

### 2.3 Numerical Refocusing

The classical angular spectrum (AS) method was used to propagate the wavefield the desired reconstruction distance. This method is a numerical integration technique that was previously developed in MATLAB® [3], [4] and this thesis purely implemented the code in experimental instrumentation setups as a black box. It is, however, important to understand the mathematical concept behind how numerical refocusing was performed to appreciate the results that were recorded when the code was implemented.

First, the complex wavefield from the polarized camera sensor (Equation (17)) was decomposed into two-dimensional plane waves. The convolution integral was taken of the complex wavefield in the spatial domain:

$$U(x, y, 0) = \iint U_0(f_x, f_y) * g(f_x, f_y) df_x df_y \quad (21)$$

where  $U_0$  is the weight of the two-dimensional complex wavefield, found by taking the Fourier transform of the field, and the phase term  $g$  (see Equation (3)) at  $z = 0$  is:

$$g = e^{2\pi i(f_x x + f_y y)} \quad (22)$$

To propagate to distance  $z$ , an extra term in  $g$  was necessary to accommodate the  $z$  distance in phase (solving for  $k_z$  component of wave vector magnitude  $|k|$  in Equation (5) and knowing  $k_{x,y,z} = 2\pi f_{x,y,z}$ , where  $f$  denotes the spatial frequency), the resulting  $g$  was calculated as:

$$g = e^{2\pi i(f_x x + f_y y + z_{rec} \sqrt{\lambda^{-2} - f_x^2 - f_y^2})} \quad (23)$$

The wavefield at a distance  $z$  therefore is:

$$U(x, y, z_{rec}) = \iint U_0(f_x, f_y) e^{2\pi i(f_x x + f_y y + z_{rec} \sqrt{\lambda^{-2} - f_x^2 - f_y^2})} df_x df_y \quad (24)$$

The expression in Equation (24) can be written using Fourier transforms. The Fourier transform of the wavefield was taken to decompose it into plane waves. This was multiplied by the Fourier transform of the phase term  $g$  to reach the Fourier transform of the wavefield at a distance  $z_{rec}$ ; the inverse Fourier transform was then performed to get the wavefield at the desired propagation distance  $z_{rec}$  back with Equation (25):

$$U(x, y, z_{rec}) = FT^{-1} \left\{ FT\{U(x, y, 0)\}(f_x, f_y) * FT\{g(x, y, 0)\} \right\} \quad (25)$$

where  $f$  denotes the complex wavefield and  $FT$  is the Fourier transform. Figure 18 shows the application of the AS method on a simulated complex wavefield of a photo of a toddler and baby, before and after numerically refocusing to the correct, sharp image at reconstruction distance  $z_{rec}$ .

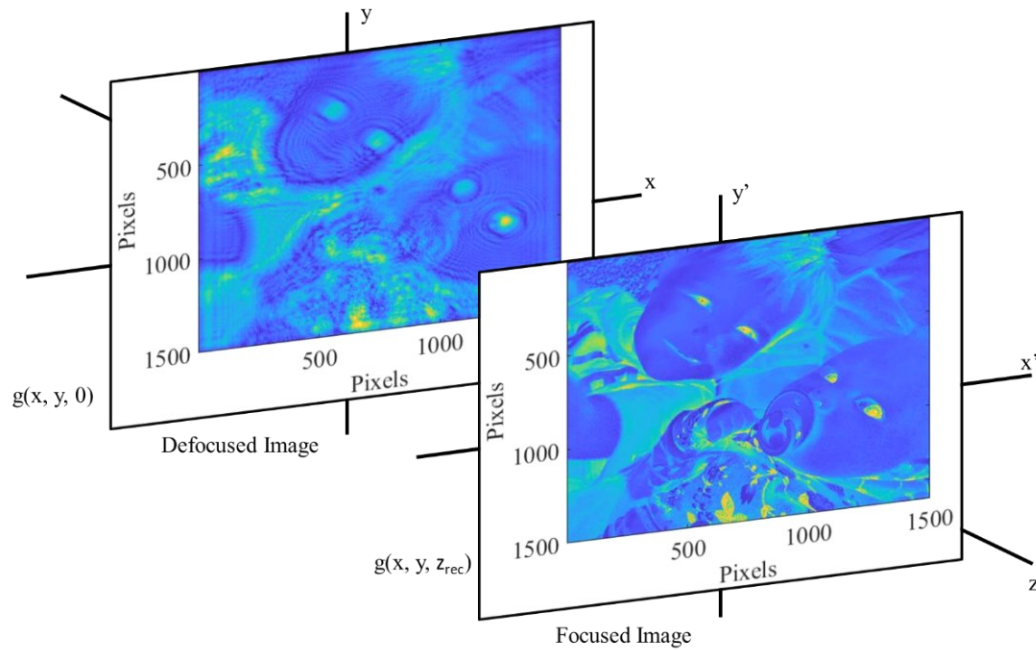


FIGURE 18: Visual representation of using the Angular Spectrum Method to numerically focus to a sharp image at distance  $z_{rec}$ .

## 2.4 Reconstruction Results

As stated, the reconstruction of an image at the desired distance was done utilizing a previously developed wave propagation/numerical refocusing algorithm [3], [4]. An implementation of this using the GP lens system is shown in Figure 19 with a figurine of the famous Socrates. The left image is the amplitude of the complex hologram before numerically refocusing. The right, clearer image of Socrates' face shows reconstruction after the algorithm was utilized to propagate the required  $z$  distance calculated from Equation (21).

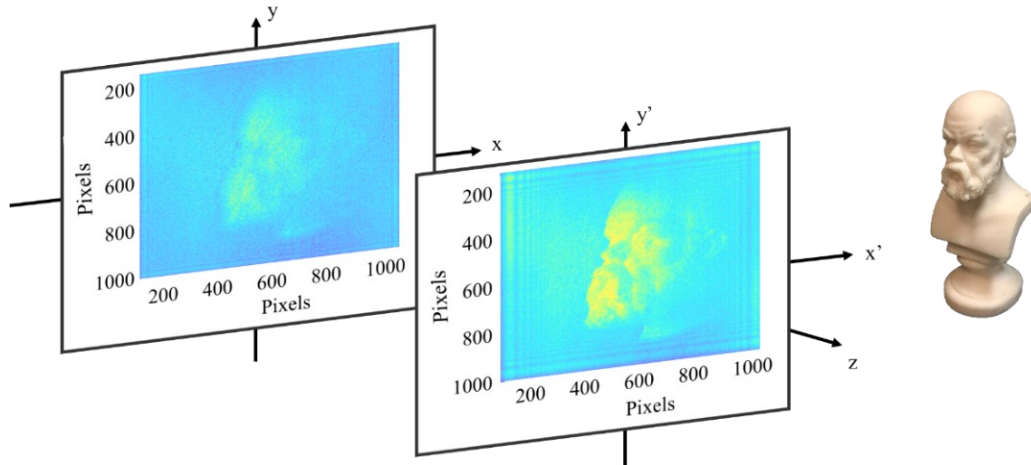


FIGURE 19: Experimental results with arbitrary color map after numerically refocusing to the face of a Socrates figure.

The wave propagation/numerical refocusing algorithm was also utilized on a planar, scattering surface that was illuminated with green stripes, shown in Figure 20.

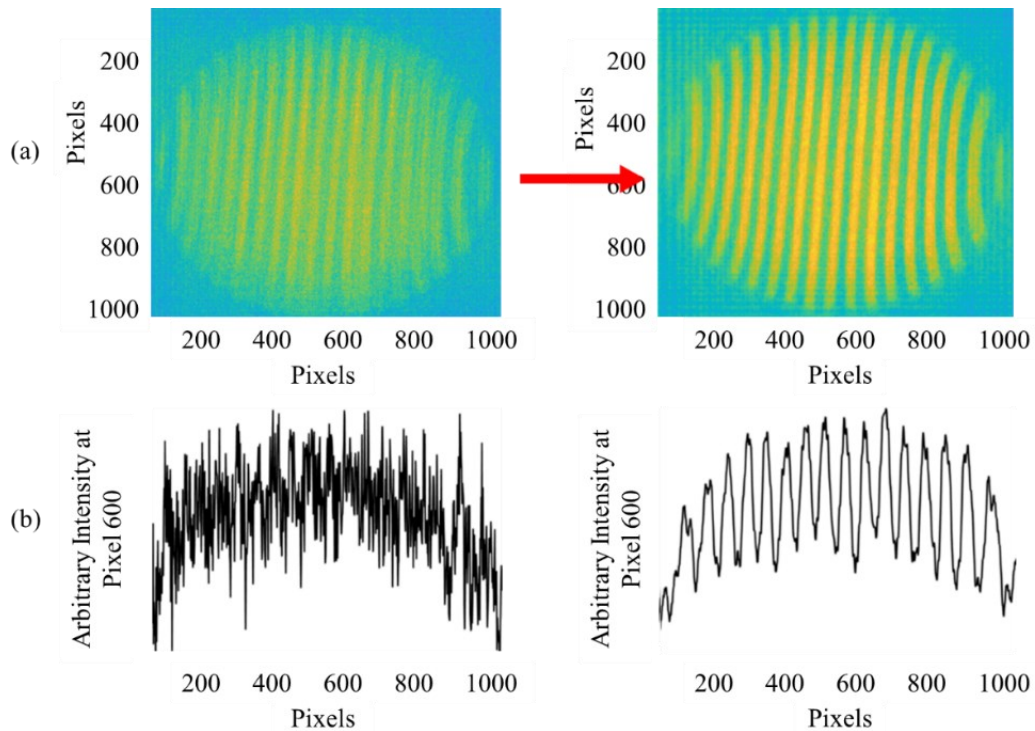


FIGURE 20: (a) Reconstruction with arbitrary color map before and after numerical refocusing of a fringe pattern projected onto a viewing screen and (b) cross-section of intensity values halfway through the image.

The reconstructed images before and after numerically refocusing are shown in Figure 20 (a), and Figure 20 (b) shows how the contrast improved in the stripes after refocusing by graphing a horizontal cross-section of the intensity values.

## 2.5 Tested Parameters

Parameters of the GP lens system that were evaluated include the field of view, resolution, and effective pixel size. These parameters are important to consider in any interferometer or holographic system to understand its performance. The method by which each parameter was evaluated is discussed.

The field of view (FOV) was evaluated at two different conditions: at different positions of the relay lens, and at different positions of the object relative to the objective lens. A dot target was utilized to observe the output FOV. The target is shown in the bottom left image of Figure 21 and the bottom right image shows where the target was placed in the experimental setup. A white light source was placed at an angle on each side of the target to allow for only scattered, incoherent light to enter the system, also shown in the right image of Figure 21.

As discussed previously in the description of the GP lens setup (see Section 2.2), a relay lens was placed in front of the polarized camera sensor to adjust the magnification of the final image. The relay lens (outlined in green in the top image of Figure 21) was moved 3 times from left to right and FOV measurements were recorded from knowing the physical distance between dots on the target.

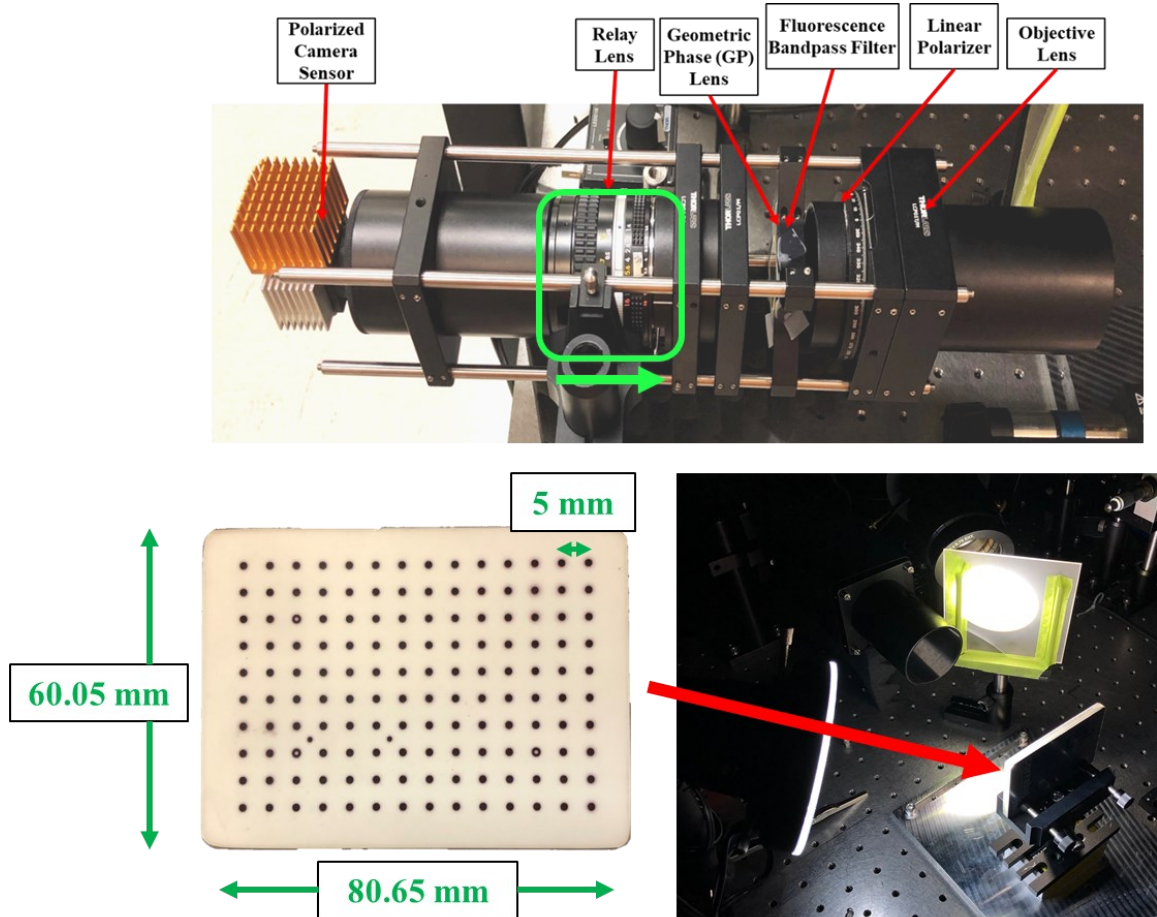


FIGURE 21: Experimental setup to calculate the field of view; top image outlines the relay lens and the direction it was moved in green; the bottom left image is the dot target with specified dimensions; the bottom right image is the experimental setup with dot target and angled illumination.

The relay lens was moved and recorded with respect to its distance from the camera, labeled  $z_h$ , and the object was moved and recorded with respect to the objective lens, labeled  $z_o$  (see labeled distance in Figure 17). Figure 22 displays the relationship between FOV when changing  $z_h$  and  $z_o$ . As shown in Figure 22, the FOV increased as the object distance ( $z_o$ ) increased. When evaluating the influence of the position of the relay lens ( $z_h$ ), with an increase in distance between the camera and relay lens, there was a general trend of a decrease in FOV.

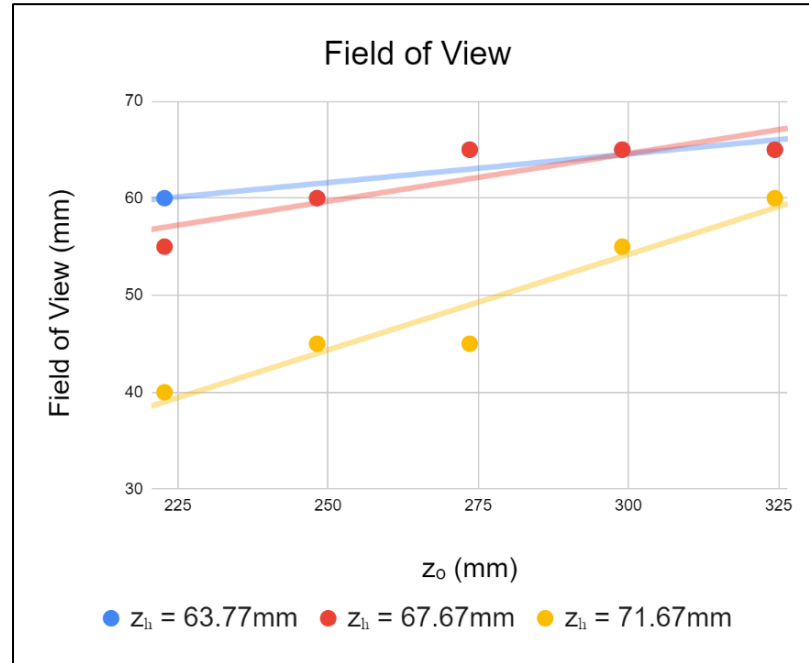


FIGURE 22: Distance between object and objective lens ( $z_o$ ) versus FOV and the comparison of the position of the relay lens with respect to the polarized camera sensor ( $z_h$ ).

The effective pixel size, defined as the number of pixels that make up the final image or capture the image data, was also evaluated [28]. This was calculated by capturing the complex wavefield of the dot target, reconstructing the dot target through MATLAB®, and physically counting the number of pixels between two dots of the dot target. The number of pixels was divided by the known distance between dots on the target (5 mm). It can be seen in Figure 23 that when the distance between the camera and relay lens increased, the effective pixel size decreased. With increased object distance from the system, there was a slight increase in effective pixel size.

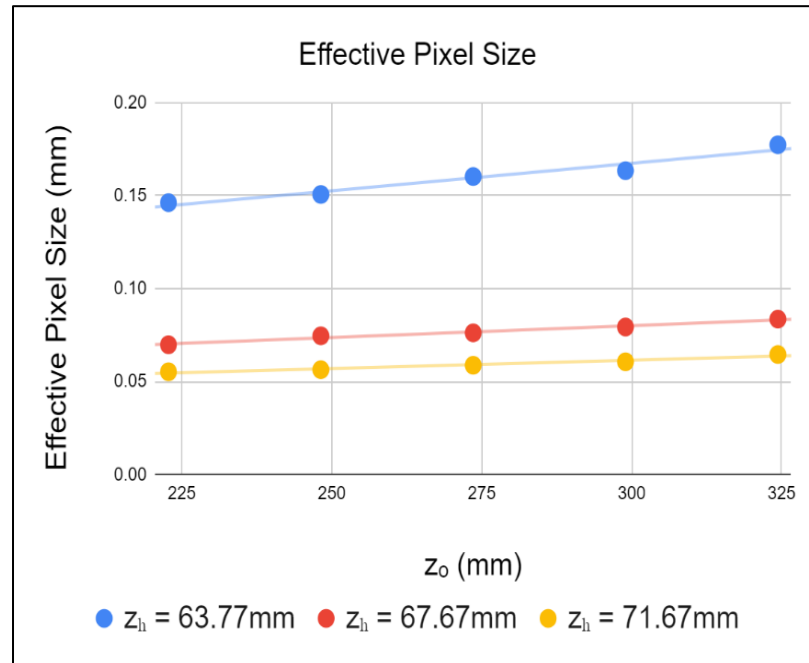


FIGURE 23: Distance between object and the system versus effective pixel size and the comparison of the position of the relay lens with respect to the polarized camera sensor.

The resolution was evaluated using a USAF-1951 target. This target consisted of groups of three-line pairs, horizontal and vertical, in a step-wise assortment, which allowed for the evaluation of precise spatial frequency. The step-wise groups of line pairs decreased in size as the group number increased and the resolution result improved based on the ability to distinguish the line pairs with higher group numbers. The reconstructed amplitude of the hologram recorded from the GP lens system is shown in Figure 24.

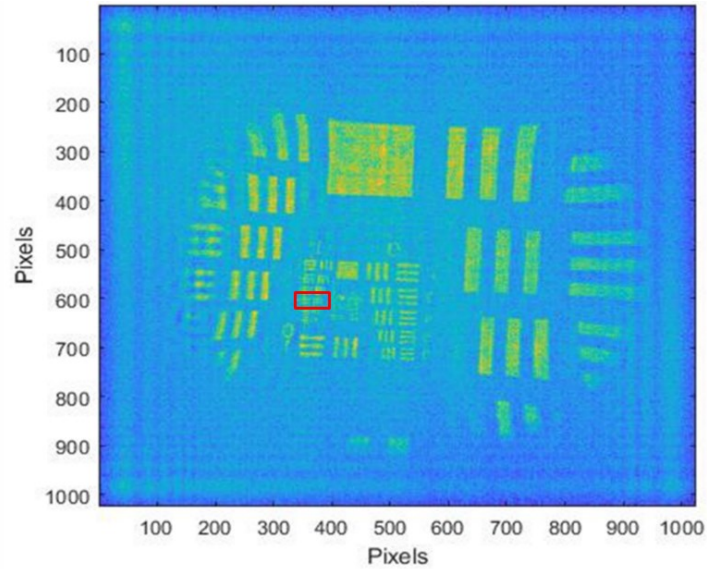


FIGURE 24: Reconstruction of an USAF-1951 resolution target using GP lens system with arbitrary color map. Outlined in red is the smallest group and row of distinguishable line pairs.

The group of lines that can be distinguished by eye in the reconstructed image are correlated with a given resolution value in a conversion chart given with the target. The units of the resolution for this target are in line pairs per millimeter, meaning it is a measure of spatial resolution, distinguishing how small of a space one can perceive in the output image. For this system, the resolution determined with the USAF-1951 target was approximately 2.83-line pairs per mm.

## 2.6 Multi-Focus Image Fusion

A goal for this project was to capture and combine multiple images at different depths through numerical refocusing and create an artificial image with all planes in focus. This application has the potential to overcome the tradeoff between depth of field (DOF) and resolution. DOF refers to the amount of distance or depth that is in focus, or clear and sharp. The relationship between DOF and resolution is inversely proportional, therefore with increasing DOF there is typically a decrease in resolution in the output

image. This tradeoff is not ideal and therefore the method of multi-focus image fusion was deployed to overcome this inverse property. An experimental setup was built and the numerical refocusing/wave propagation algorithm [3], [4] followed by an image fusion algorithm [26] was utilized to perform multi-focus image fusion.

### 2.6.1 Experimental Setup

To measure varying depths at once, a white diffuse screen angled with respect to the system was placed in front of the setup (see top image in Figure 25).

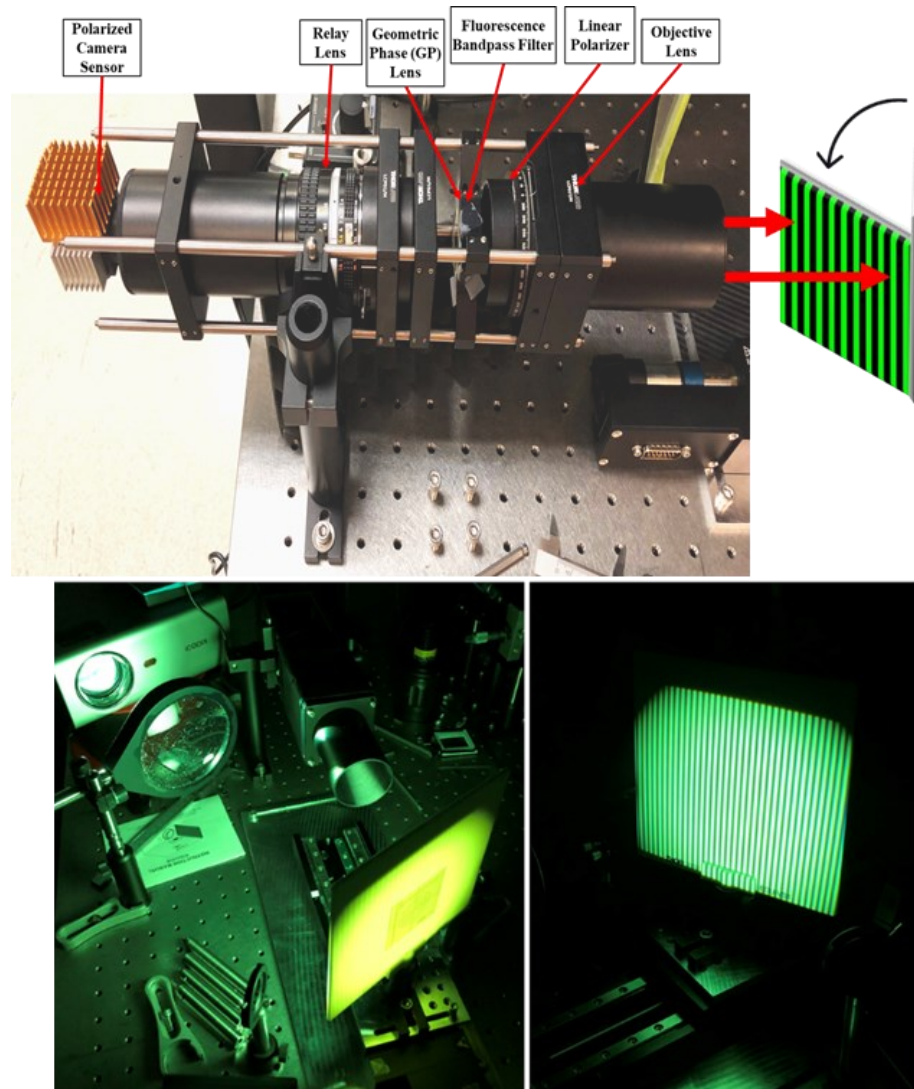


FIGURE 25: Experimental setup of allowing the system to be exposed to multiple depths to perform multi-focus image fusion.

A projector illuminated the screen with green stripes. In the bottom-left image, the entire experimental setup is shown, consisting of a projector and a focusing lens to produce stripes onto the angled screen. The bottom right image shows the striped pattern that is projected onto the screen.

### 2.6.2 Results

Figure 26 (a) shows the two images that were captured at a short and far distance of the screen on the left, and the red boxes indicate where the images are in focus. Figure 26 (b) shows the amount of contrast in the fringes by capturing a cross-section of the horizontal intensity data, halfway through the image. As shown, there was higher contrast in the areas in focus. The right final image in Figure 26 (a) displays the artificial, combined image output using the multi-focus image fusion algorithm [26], [27].

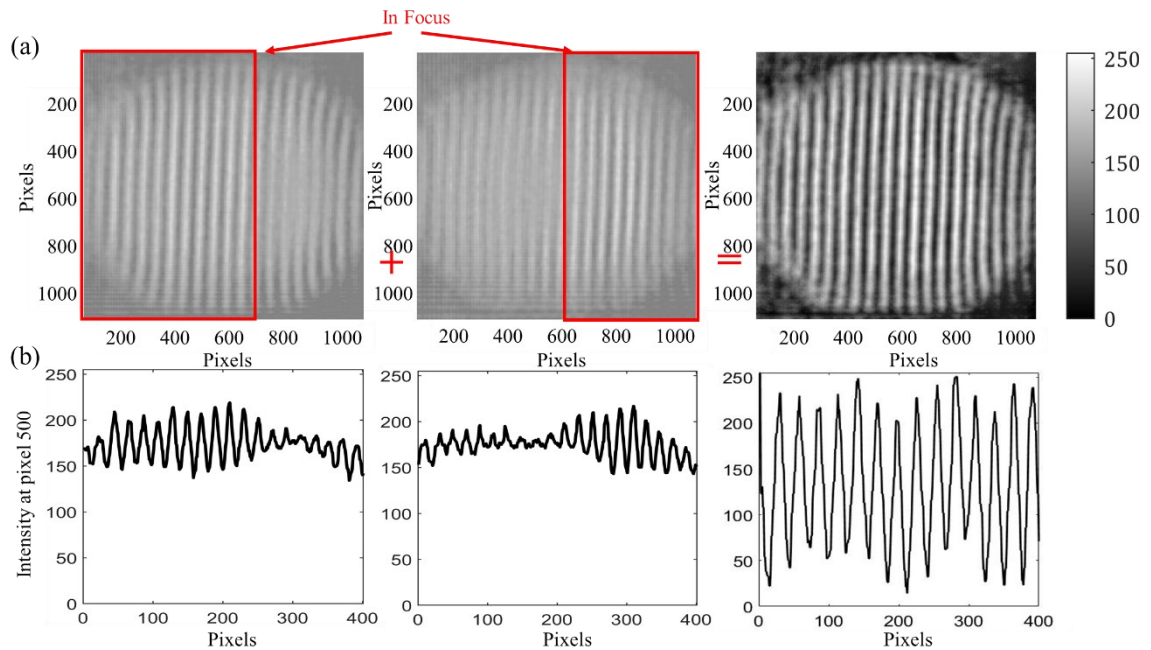


FIGURE 26: (a) Results of performing multi-focus image fusion with the sum of images focused at different depths (with grayscale intensity colorbar), and (b) the contrast of fringes across the 500th pixel (halfway through image).

The contrast drastically improved across the entire image after running this algorithm, due to its exposure correction properties, and all stripes at all depths were in focus.

## CHAPTER 3: EXPERIMENTAL SETUP AND PROCEDURE – GP GRATING

### 3.1 Introduction

Previous setups of lateral shearing interferometers include expensive and fragile components such as a Wollaston prism, or a double-focus interferometer, etc. [29]. Proposed is a new method of incoherent variable shearing interferometry using a less expensive component, the GP grating (See Section 1.7.2). Recall that LHCP and RHCP passing through a GP grating diffracts into positive and negative 5 degrees from the optical axis. This shift results in two copies of the image slightly displaced from one another, causing a shearing effect. In the proposed setup, the amount of shear can be adjusted, and thus the fringe period, using a 4f configuration with two lenses and another GP grating. The system is called 4f due to the total distance of the system being four times the focal length of the lenses (see labeled distances in Figure 27 (a)).

The 4f configuration is shown in Figure 27. Three different positions of the second grating are shown, which directly shows that the shear can be easily adjusted in this manner. In Figure 27, linearly polarized light enters the first GP grating from the left, splits based on its circular polarizations at plus and minus 5 degrees, and the first lens collimates the light. The light then travels two times the focal length of the lenses, and then reaches the second lens to refocus the light.

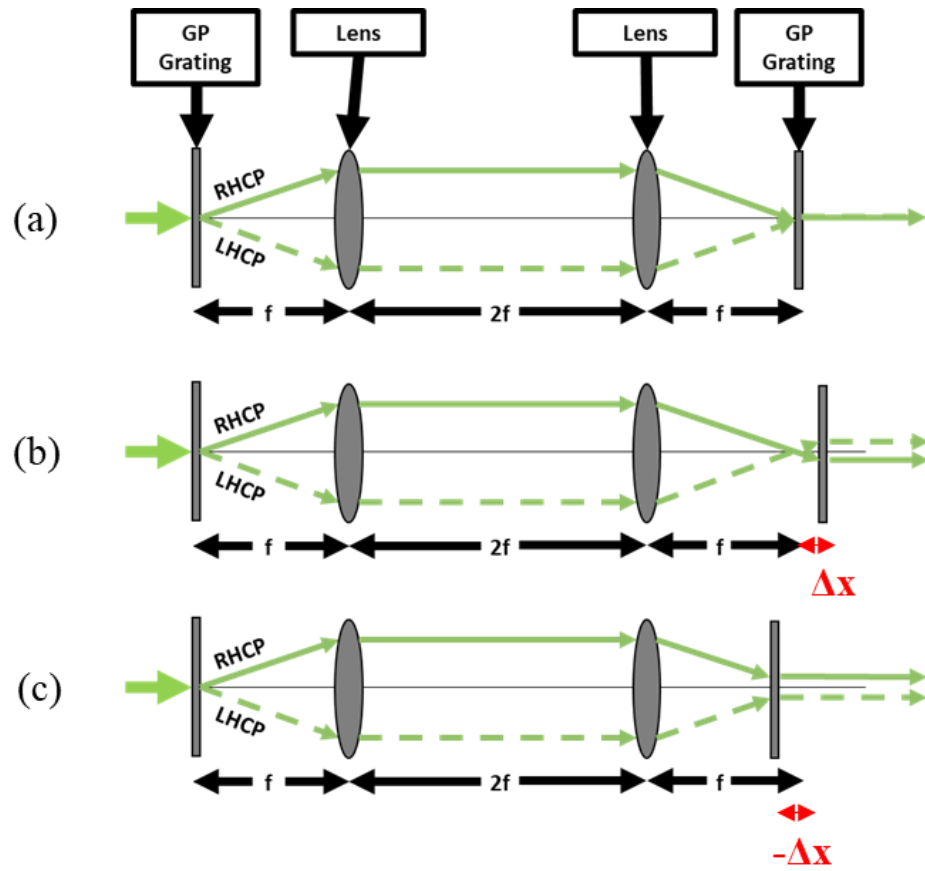


FIGURE 27: Schematic of 4f system of GP gratings and lenses. (a) Gratings are placed at the focal length of the lenses. (b) Right grating is moved outside the focal length of the lens a distance  $\Delta x$ . (c) Right grating is moved inside the focal length of the lens a distance  $f - \Delta x$ .

In Figure 27 (a), the second grating is placed directly at the focal length of the lens, resulting in perfect overlapping of the two copied images, therefore no shearing occurs. In Figure 27 (b) the second grating is placed a small distance after the focal length, denoted in red, resulting in a small shear of the two images. In Figure 27 (c), the grating is just before the focal length of the lens, which, as shown, is another way to create a shear. The two offset wavefronts interfere with each other, creating an interferogram at the camera sensor [30]–[33].

### 3.2 Experimental Setup

In shearing interferometry using incoherent illumination, if the object is placed in the Fourier plane, it allows both spatially shifted wavefronts to interfere, due to the light from the object behaving as a point source, enabling spatial coherence [21]. The correct distances to be in the Fourier domain, the experimental setup, and schematic of components are shown in Figure 28. The arrows in the bottom schematic show how the light is manipulated as it passes through each component of the system.

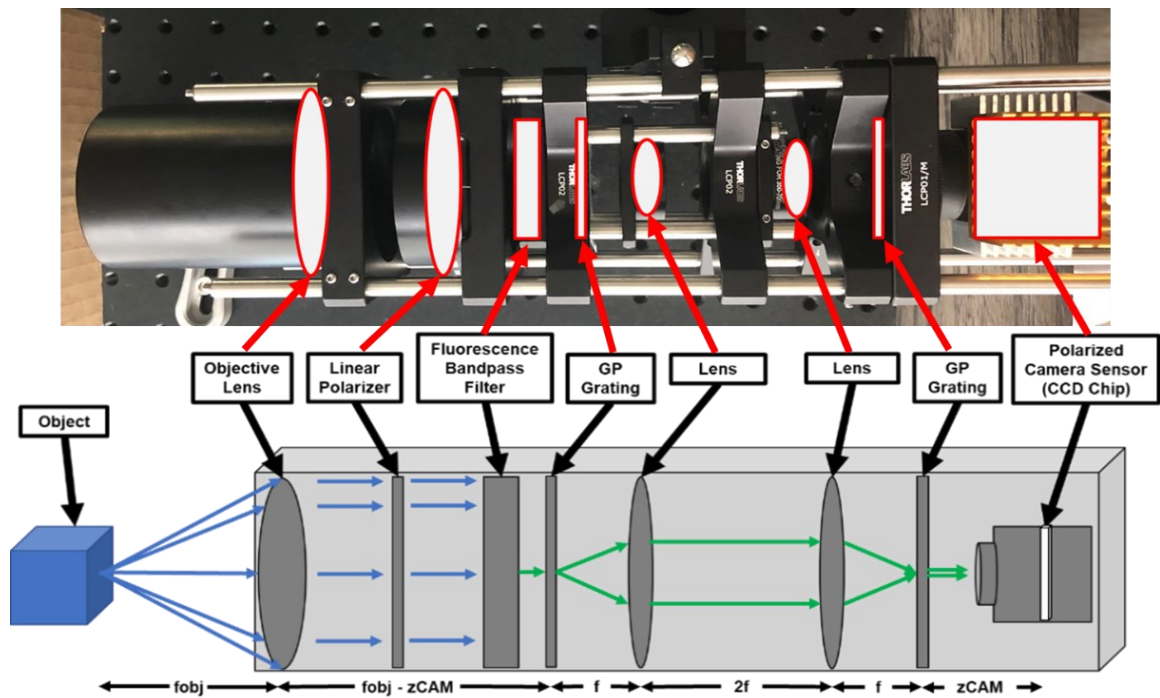


FIGURE 28: Experimental GP grating setup (top) and schematic (bottom) for Fourier domain reconstruction;  $f_{obj}$  is the object distance and focal length of the objective lens;  $z_{CAM}$  is the distance between the second grating and camera sensor;  $f$  is the focal length of the two lenses in the  $4f$  system.

An object was placed at the focal length of the objective lens, where the distance is denoted as  $f_{obj}$  in Figure 28. Here, the object was placed in the Fourier plane and thus behaved as a point source, where the objective lens took each point of the object and

made it spatially coherent. The light then passed through a linear polarizer, which only allowed 0-degree linearly polarized light to pass through the rest of the system, which was analyzed as 50% LHCP and 50% RHCP. The next component was a fluorescence bandpass filter of 520 nm with 10 nm bandwidth, allowing for an increase in temporal coherence. The light then entered the 4f configuration shown in Figure 27, and then reached the polarized camera sensor at a distance  $z_{CAM}$  from the second grating.

The gray box in the bottom schematic of Figure 28 is denoted as the incoherent wavefront sensor. To analyze how the Fourier system behaves with a single point source, a pinhole was created and placed in front of the system by drilling a hole into a piece of cardboard, as shown in Figure 29. The light source from the spotlight has a coherence length of  $27\ \mu\text{m}$ . To achieve incoherence, a diffuser was placed directly after the light source to scatter the light.

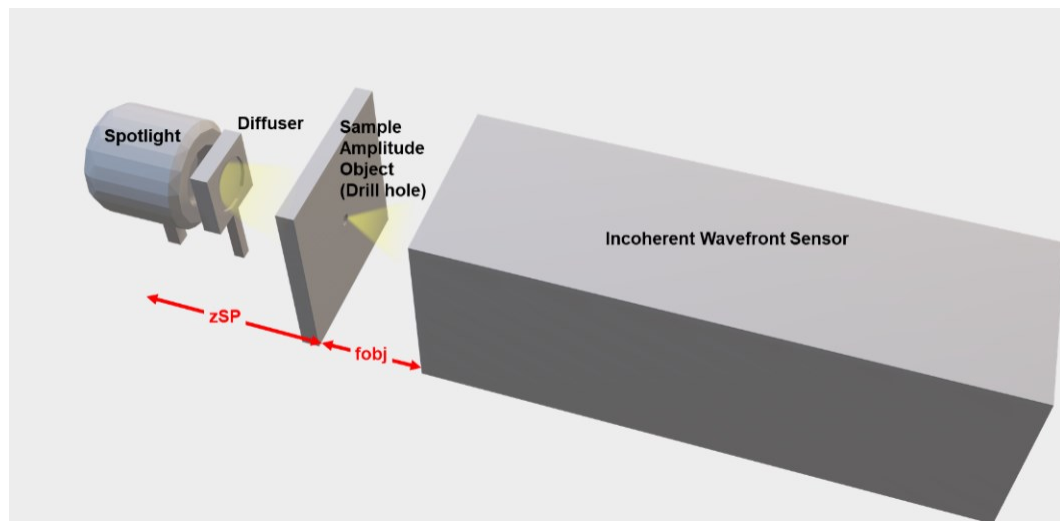


FIGURE 29: Pinhole experimental setup where  $z_{SP}$  depicts the distance between the spotlight and pinhole and  $f_{obj}$  is the distance between the pinhole and the incoherent wavefront sensor and focal length of the objective lens.

### 3.3 Results

Figure 30 shows the resulting fringes that were captured in the pinhole setup after calculating the phase of the wavefront in MATLAB® at different positions of the second grating (in the 4f configuration Figure 27 (b) and (c)).

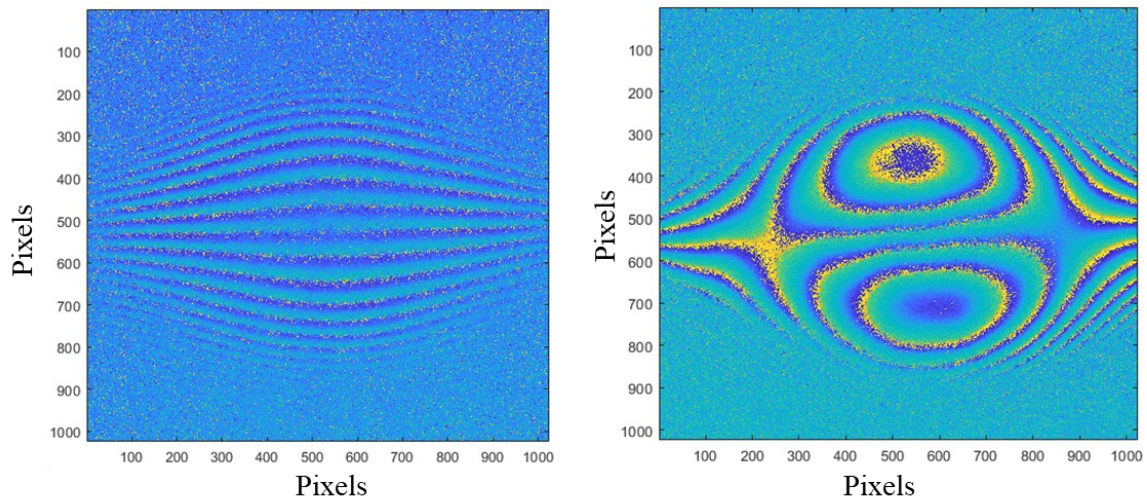


FIGURE 30: Different fringe patterns obtained when changing the position of one of the gratings in the pinhole configuration of the GP grating setup with arbitrary color map.

The pinhole was illuminated with coherent, incoherent, and partially coherent light to see how the system behaved with different levels of coherence. Based on the illumination, different outputs of the system were obtained. To achieve a coherent light source, the spotlight in Figure 29 without a diffuser in front of it was used. To experimentally recognize partially coherent light, tissue paper was placed in front of the pinhole. An additional diffuser was placed in front of the spotlight to have incoherent light.

When the pinhole was illuminated with the incoherent light source, as shown in Figure 31, the FOV was large and the contrast of the fringes was minimal. I1 through I4 in the figure shows the four intensities at the polarizations of the camera sensor (0, 45,

90, and 135 degrees). The resulting amplitude (top right) and phase (bottom right) are also displayed.

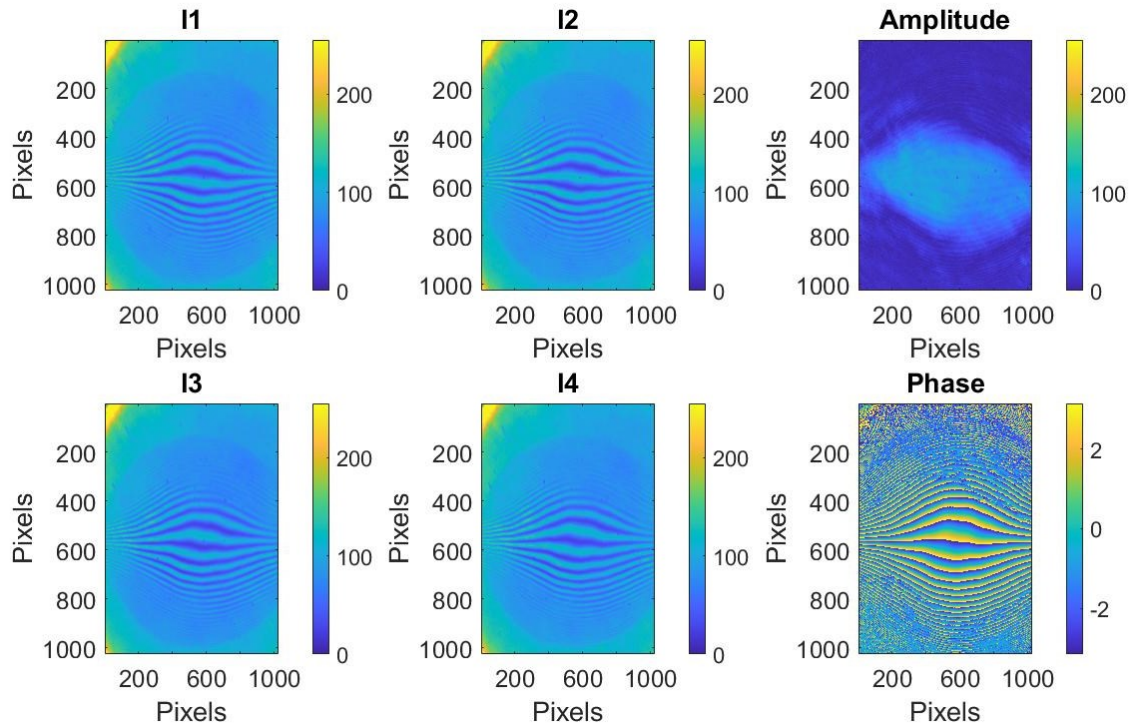


FIGURE 31: Results of fringes at different polarizations I1-I4, amplitude with intensity color map, and phase with phase color map of complex wavefield when illuminated with incoherent light.

When the GP grating system was illuminated with coherent light, the setup displayed higher contrast fringes with a narrowed FOV, as shown in Figure 32. It is speculated that the square outline in each output is related to the square geometry of the pinhole.

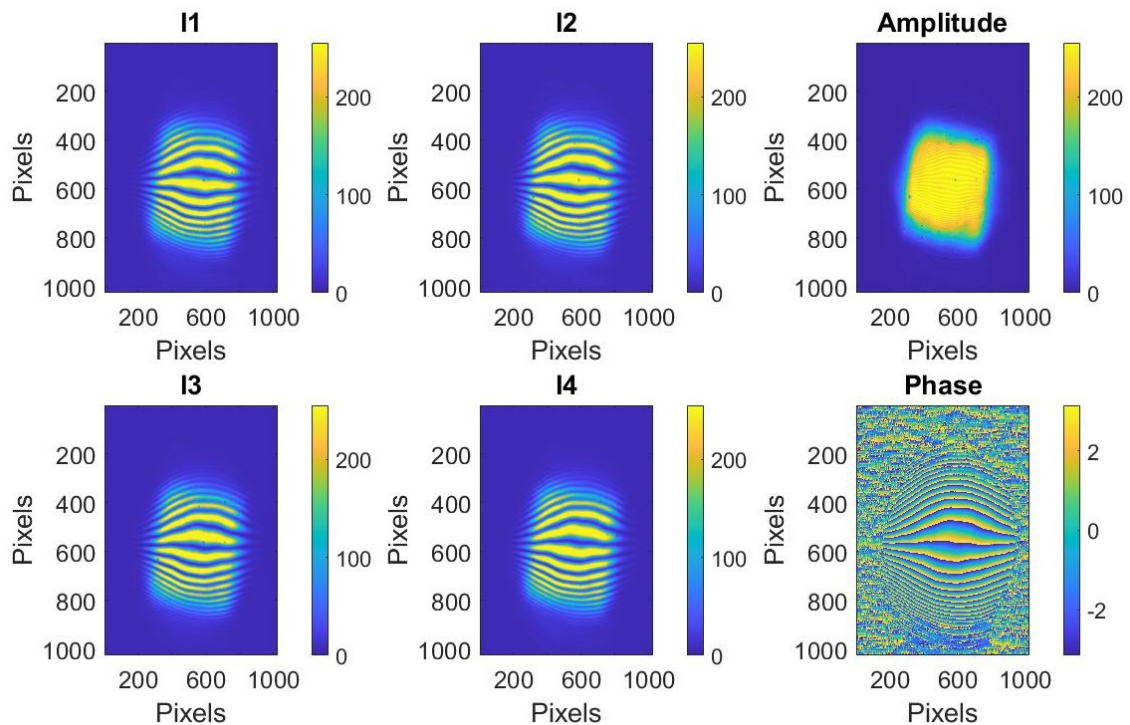


FIGURE 32: Results of fringes at different polarizations I1-I4, amplitude with intensity color map, and phase with phase color map of complex wavefield when illuminated with coherent light.

When the pinhole was illuminated with partially coherent light, the results are shown in Figure 33. The field of view expanded to the edges similar to the incoherent light source, however, the fringes had low contrast, which may be due to the exposure time of the camera sensor. It was shown that this setup worked with incoherent, coherent, and partially coherent light in that it did not modify the resulting fringe pattern.

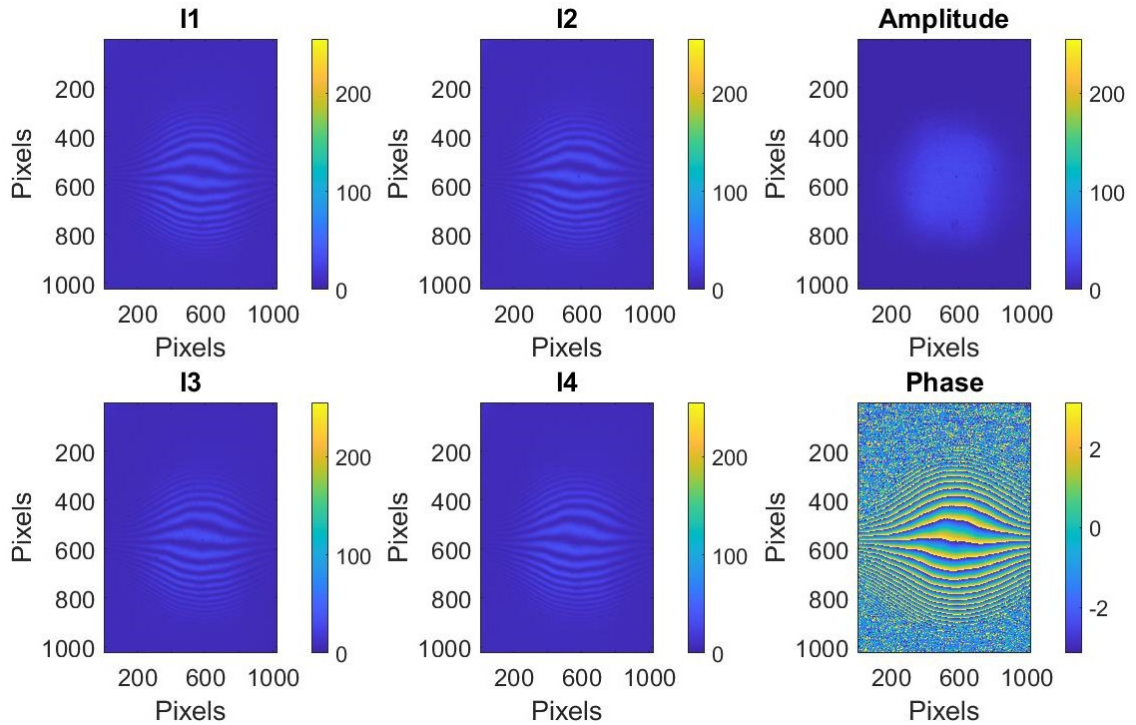


FIGURE 33: Results of fringes at different polarizations I1-I4, amplitude with intensity color map, and phase with phase color map of complex wavefield when illuminated with partially coherent light.

The GP grating setup was modified to determine the resolution of the output amplitude of the hologram by placing the object in the spatial domain, or where the image is formed (as opposed to the Fourier domain). To achieve this, a relay lens was placed before the camera to control the magnification and the objective lens at the beginning of the system was removed. The 4f configuration, the linear polarizer, and fluorescence bandpass filter remained the same as the Fourier configuration. When reconstructing an USAF-1951 resolution target, Figure 34 shows the resulting sum of intensities I1 through I4 of all polarizations in the right image. The experimental setup is shown in the left image. The results showed that the image had less speckle and generally looked better than the GP lens setup, with a resolution value of 8.98-line pairs per mm.

However, this setup had a higher magnification, which needed to be realized when comparing the two setups in terms of resolution.

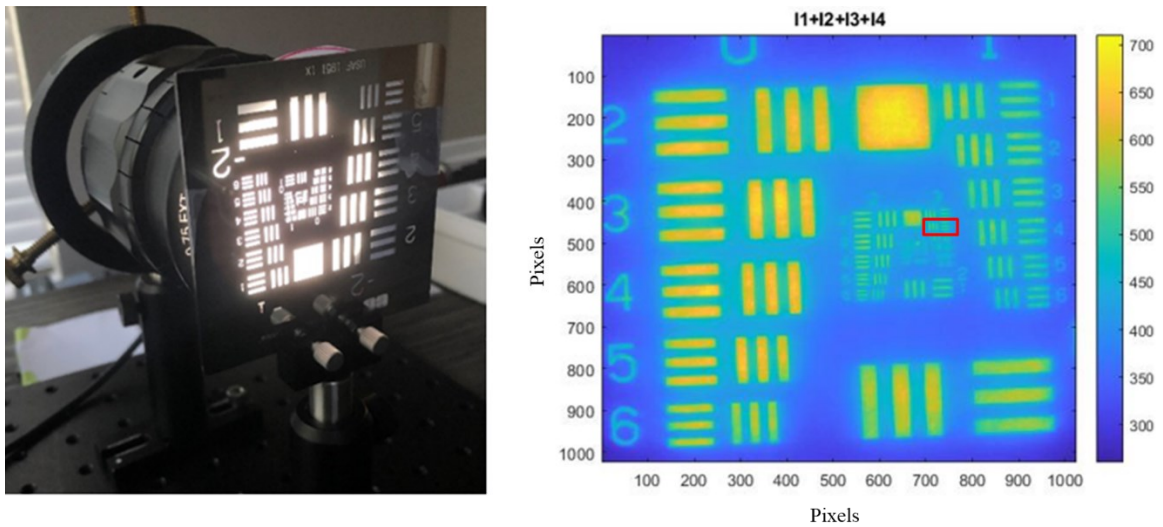


FIGURE 34: Experimental setup of USAF-1951 target (left) and reconstruction results (right). Outlined in red is the smallest group and row of distinguishable line pairs.

### 3.4 Comparison of GP Lens and GP Grating Experimental Setups

When comparing the different experimental setups of the GP lens (Chapter 2) and GP grating setups, as previously stated, it is first important to realize that there was a clear magnification difference between the two systems, as shown in Figure 35. The magnification of the GP grating setup (bottom right image) was about four times that of the GP lens setup (left image). In terms of FOV, the GP lens setup had a FOV of approximately 19.4 mm and the GP grating setup was 6.45 mm. The magnification influenced the resolution result because due to the image being smaller, it was consequently harder to distinguish between line pairs.

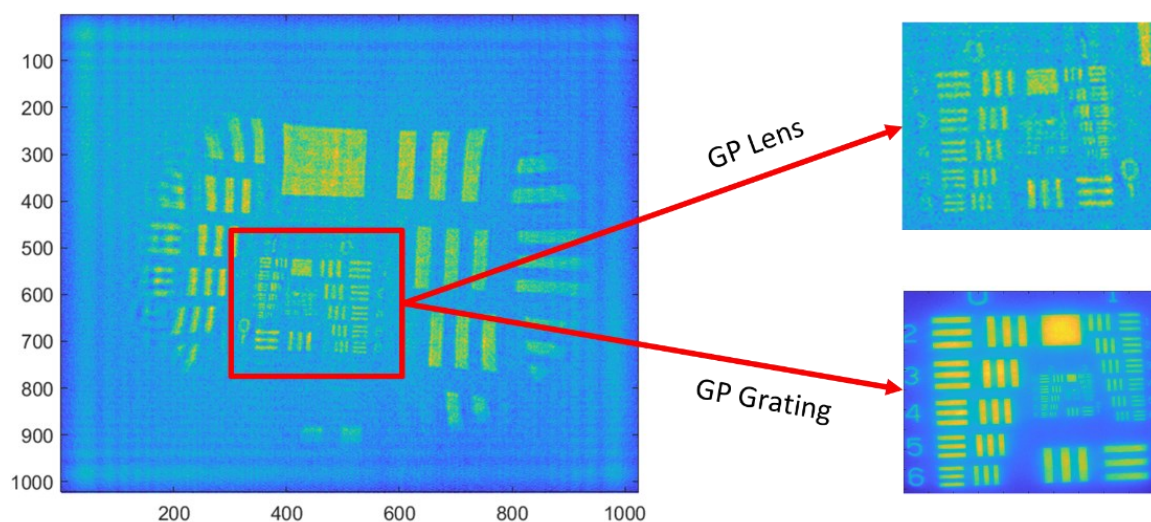


FIGURE 35: Comparison of USAF-1951 resolution target reconstruction using GP lens setup (left and top right image) and GP grating setup (bottom right).

To numerically compare the two setups, the systems would have to be configured to achieve the same level of magnification. However, as a visual, non-numerical comparison, the red squared section in the GP lens setup on the left of Figure 35 was cropped and placed next to the reconstructed output of the GP grating setup (top right). Visually, when comparing the two systems, the GP grating setup produced nicer looking results, with less speckle and the ability to distinguish more line pairs as opposed to the GP lens system.

## CHAPTER 4: COMPACT INTERFEROMETER USING COHERENT LIGHT

### 4.1 Introduction

As technology continues to advance, devices are becoming more compact. This is no exception in the field of optical metrology, especially in its application to a manufacturing environment. However, the demands of performing digital holography have hindered the compactness in such setups [2]. Therefore, the goal of this project was to make a compact, handheld interferometer system. To achieve stability, the system was self-referenced and common path, similar to the previous chapters' setups, and the use of the GP grating made the system more compact than traditional holographic systems.

Three different setups were numerically evaluated (see Appendix B) and modeled to determine their capabilities based on the types of surfaces they were intended to measure and their level of compactness. Each setup in this chapter used a coherent light source. Experimental setups 1 and 3 were developed to measure reflective or polished surfaces and setup 2 was developed to measure rough surfaces. Each setup had its advantages and disadvantages, which are discussed in the following sections.

### 4.2 Setup 1

A similar setup to the previous GP grating system (Chapter 3) was built with a slight modification in terms of illumination and position of the object. The system was intended to measure reflective or polished surfaces. To measure reflective surfaces, the setup includes a beamsplitter, so the angle of illumination is perpendicular to the surface of the object. Therefore, the reflection from the object surface can directly enter the system to be measured. The schematic of setup 1 is shown in Figure 36 (a). This system setup consists of a laser light source, a half-waveplate, a linear polarizer, a beamsplitter,

the GP gratings and lenses 4f configuration, a magnification lens, and a polarized camera sensor.

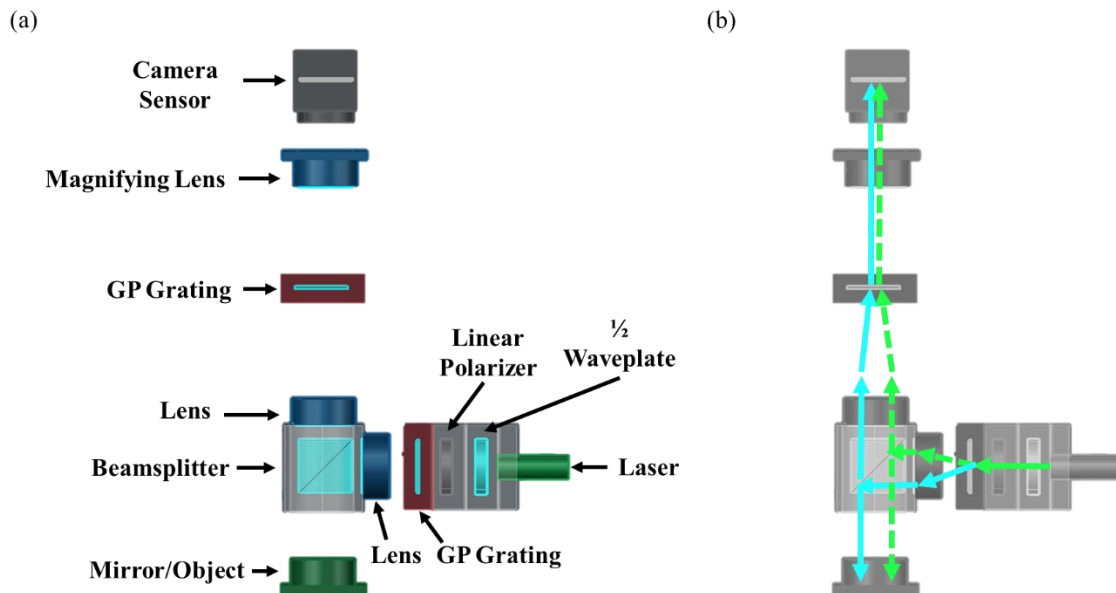


FIGURE 36: (a) Schematic of compact interferometer: setup 1 consisting of a 4f configuration and (b) ray diagram.

A ray diagram of how the light propagates is shown in Figure 36 (b), and a more detailed schematic of the shifted wavefronts are shown in Figure 37. The laser light first propagates through a half-waveplate. A half-waveplate creates a phase shift of half the wavelength [34], therefore it can be rotated to adjust the incoming polarization to be 0-degree polarized light. The light then propagates to the linear polarizer, which ensures that strictly linearly polarized light at 0 degrees enters the first grating, which diffracts the light plus and minus 5 degrees based on their circular polarizations. The separated wavefronts propagate to the first lens, which collimates the light, and then the collimated wavefronts reach the beamsplitter, changing the direction to propagate to the object perpendicular to the surface. The light bounces off the object, and the wavefront carrying

the object surface information propagates to the second lens, which images the object onto the second grating. The second grating corrects the angle that was created from the first grating, and the magnifying lens then images the object onto the polarized camera sensor. A visual representation of the wavefront when it shears at a positive 5 degrees (RHCP, Figure 37 (a)), negative 5 degrees (LHCP, Figure 37 (b)), and both sheared wavefronts (Figure 37 (c)) are shown.

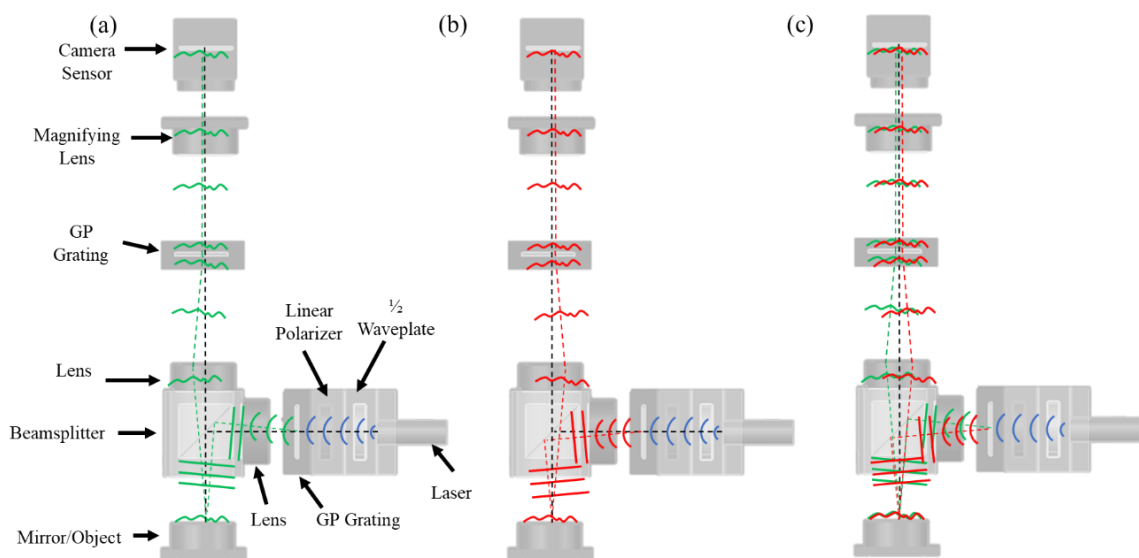


FIGURE 37: Schematic of how wavefront propagates through setup 1 with (a) shift of positive 5 degrees (RHCP), (b) shift of negative 5 degrees (LHCP), and (c) both sheared wavefronts.

Setup 1 was built and tested to see if interference fringes could be formed in this configuration experimentally, shown in Figure 38. While waiting for a fiber optic laser to arrive, readily available components were utilized to test this setup. These components included a 1 mW laser of red wavelength and a beam expander, which expanded the wavefront in all directions as if it were a point source.

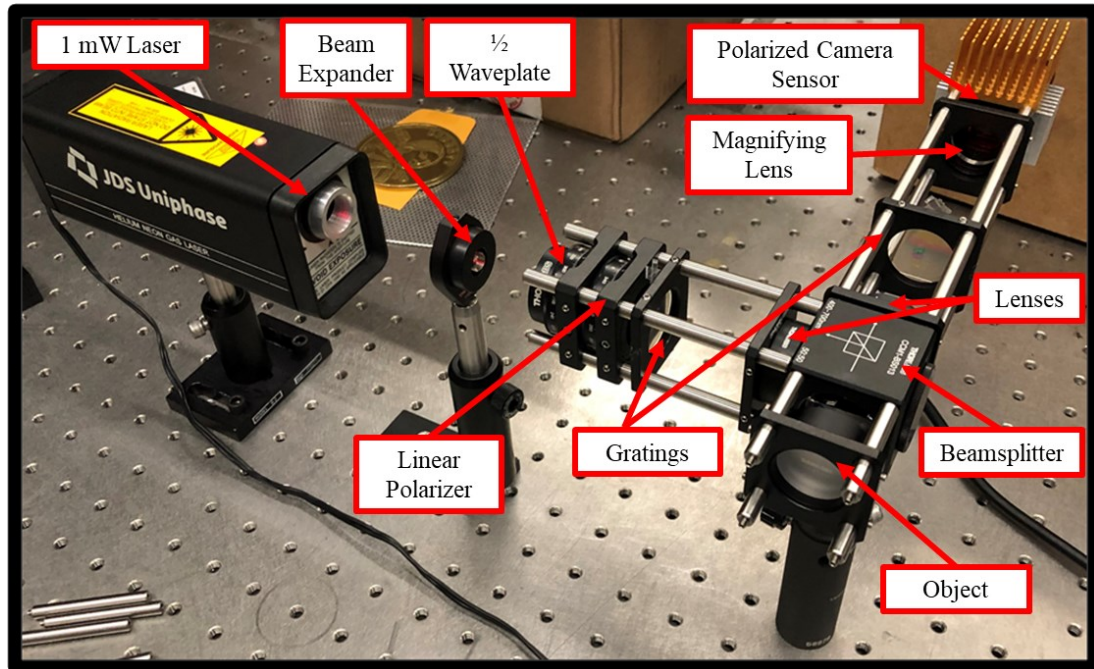


FIGURE 38: Photo of experimental setup of compact interferometer setup 1.

#### 4.2.1 Results

The ability to form interference fringes was successfully demonstrated with setup 1 and the four different intensities at polarizations I1 through I4 at the camera sensor are shown in Figure 39. An advantage of this system was that it was easy to adjust the amount of shear by moving one of the gratings. It also worked with both spatially and temporally incoherent light, therefore it will work with a variety of light sources such as white light, laser-emitting diodes (LEDs), lamps, etc. The disadvantage, however, is that this system was bulkier than the original idea, which was to have the ability to fit the entire system in the palm of a hand.

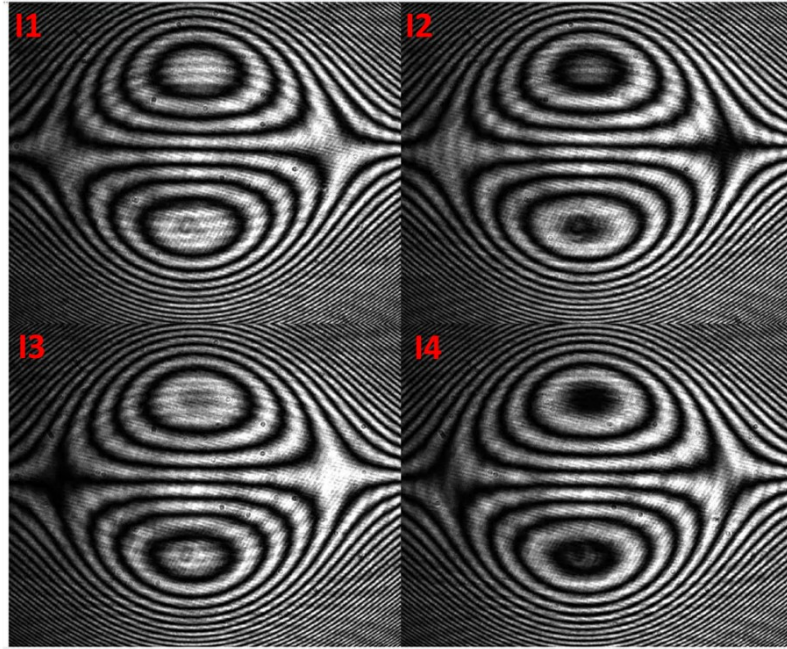


FIGURE 39: Fringe pattern results at the four different polarization angles from the polarized camera for setup 1.

With experimental setup 1, it was also possible to detect, in real-time, defects or contamination on a mirror through the camera's software, SpinView®. This is possible because SpinView® allows the option of calculating the degree of linear polarization (DoLP), which describes quantitatively the fraction of total incident light that is linearly polarized [35]. The contaminant, in this case, the dust particles on the mirror, are circled in red on the left image of Figure 40. The right image shows the output from the camera software, where the two dust particles are clearly visible, and when the mirror was rotated, the DoLP output showed in real-time the movement of the particles. An application of this ability includes quick defect detection in a manufacturing environment.

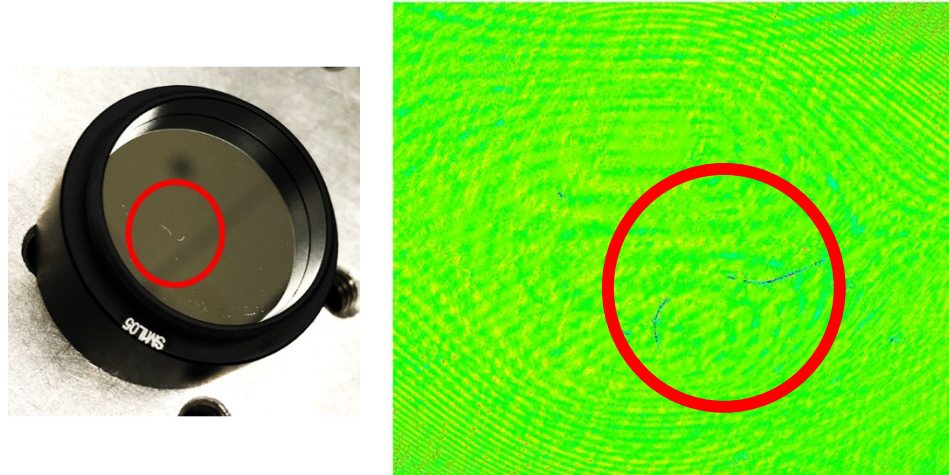


FIGURE 40: Contamination of dust on mirror (left) and degree of linear polarization output from SpinView® in real-time (right).

#### 4.3 Setup 2

Another experimental setup for a compact interferometer was to attempt utilizing one GP grating instead of two to make the system more compact. This setup was inspired by a publication by Albertazzi [36], in which they utilized a Wollaston prism, a quarter-waveplate, and a polarizer that required manual rotation to perform shearing interferometry. The Wollaston prism was what created the shearing effect in their setup by separating the incoming rays into two orthogonally linearly polarized rays [36]. Since their system had two orthogonally linearly polarized beams, they could not interfere alone, so a quarter-waveplate was introduced to convert the light to circular polarizations so that they were able to interfere after a linear polarizer [36]. Once this was achieved, their system performed relative measurements and detected small deformations using comparative measurements [36].

In setup 2, the GP grating and polarized camera sensor take the place of the Wollaston prism, quarter-waveplate, and manually rotating polarizer. This is because the

GP grating splits the light into circular polarizations directly, and the camera sensor performs single-shot phase shifting (see Section 2.2.1) as opposed to a manually rotating polarizer. Therefore, this system is more compact, can take higher speed measurements, and does not require the mechanical movement of parts. The schematic of the key principles of setup 2 is shown in Figure 41.

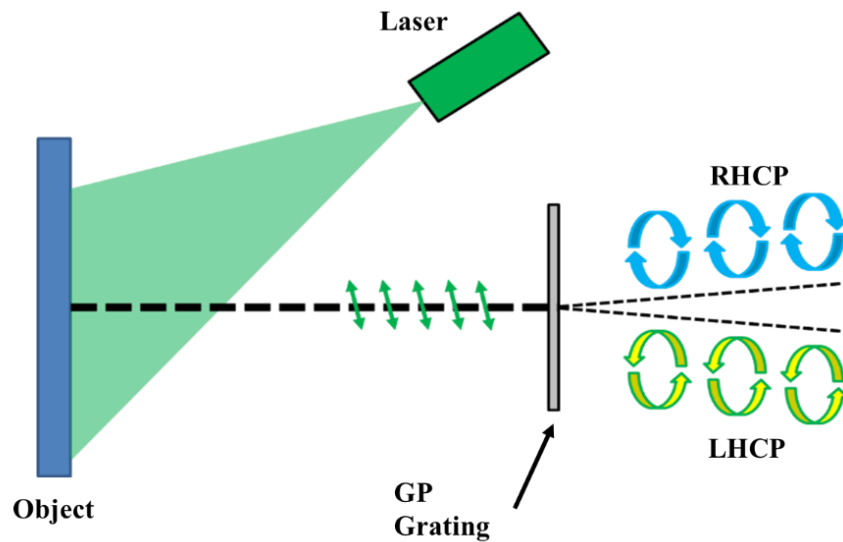


FIGURE 41: Schematic of setup 2.

The angled illumination is possible when measuring rough surfaces due to its scattering properties. When the light reaches the object, it is scattered in all directions, and as explained in Figure 9 (c), the linearly polarized portion of the light reaches the GP grating and splits the wavefront at plus and minus 5 degrees based on their circular polarizations. Then, the beams are separated and have the ability to interfere at the polarized camera sensor.

The experimental setup of setup 2 was built and consisted of a laser source, beam expander to illuminate the object, a linear polarizer to filter only 0-degree polarized light, a GP grating, and magnifying lens, shown in the left image of Figure 42. The middle

image shows the object that was measured, in this case, a barcode sticker. The resulting horizontally sheared image is shown on the right of Figure 42, which appeared speckled due to the scattered light illumination.

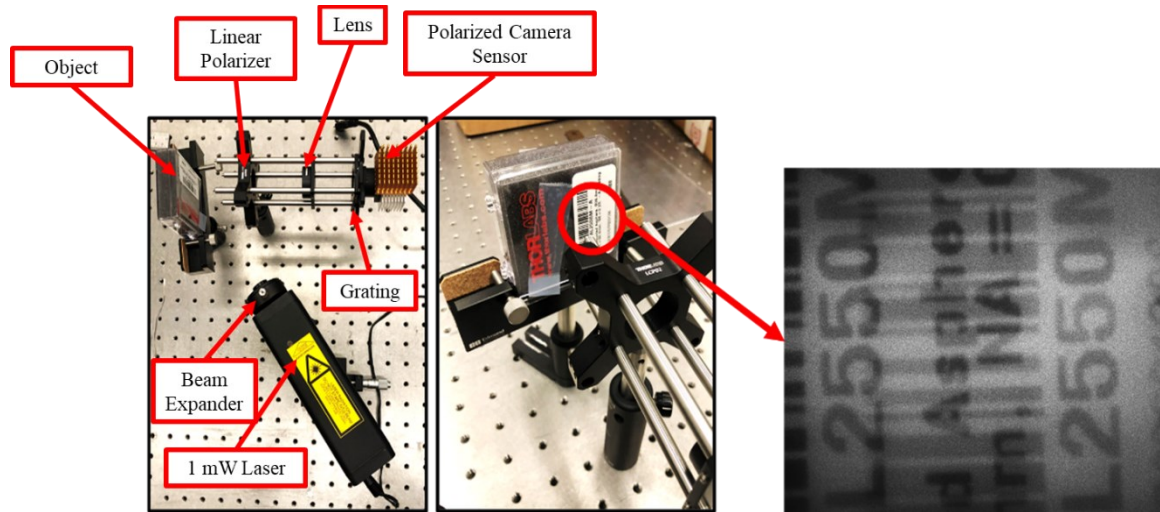


FIGURE 42: Experimental setup of setup 2 and the resulting sheared image of a barcode sticker.

Future work is required in this setup, including taking relative measurements similar to Albertazzi [36] to obtain fringes in this configuration.

#### 4.4 Setup 3

Setup 3 had the intent of a more compact system using one grating and allowing for the measurement of reflective surfaces as well. Therefore, a beamsplitter, similar to setup 1, was added to the system to allow the angle of illumination to be perpendicular to the reflective or polished sample. A schematic of setup 3 is shown in Figure 43 (a) with its corresponding ray diagram in Figure 43 (b).

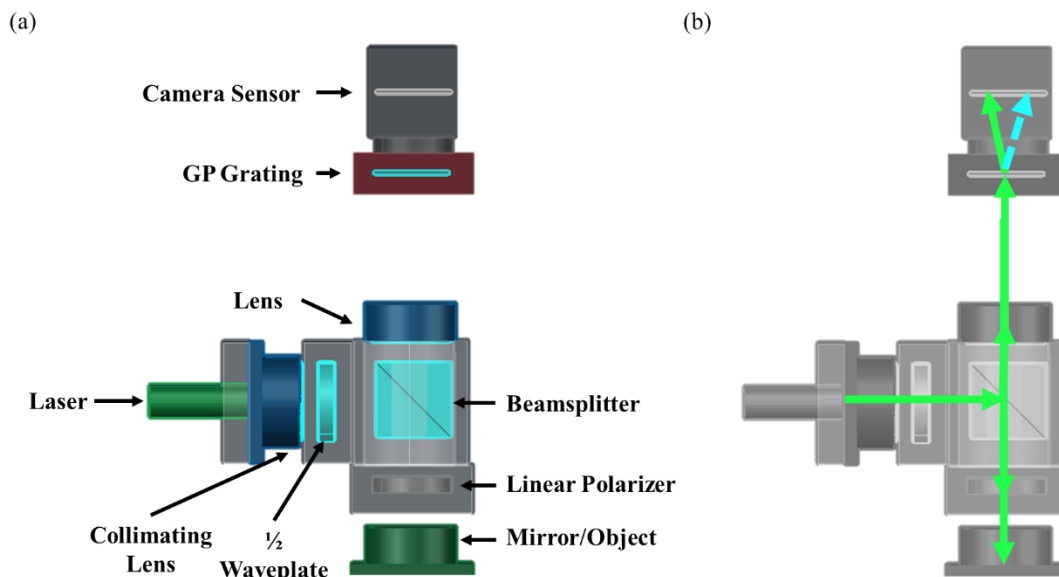


FIGURE 43: (a) Schematic of single GP grating compact setup (setup 3) and (b) ray diagram.

The laser illuminates the first lens which collimates the light. The beam then propagates to a half-waveplate to adjust for the correct polarization angle, similar to setup 1. The wavefront propagates through the beamsplitter, redirecting the light to the linear polarizer to ensure that only linearly polarized light enters the wavefront sensor. The wavefront then perpendicularly illuminates the object and reflects to the imaging lens, which images the object wavefront onto the GP grating. The wavefront is separated accordingly (see Section 1.7.2), and the two beams interfere, producing interference fringes where they overlap at the polarized camera sensor.

The advantages of setup 3 are that it is more compact and portable when compared to setup 1. However, it is not straight forward to adjust the shear because the sheared wavefronts enter the polarized camera sensor at an angle, therefore the grating position would have to be fixed and calibrated. Another disadvantage is that the setup only works with coherent light, meaning a laser source would be needed, increasing the

cost of the system. Future work to be done with setup 3 includes building the experimental setup and testing if fringes can be formed experimentally.

## CHAPTER 5: CONCLUSIONS AND FUTURE WORK

For setups intended for incoherent light, the GP grating setup from chapter 3 resulted in fewer distortions and less noise than the GP lens setup from chapter 2. The GP gratings were then utilized in the second project explained in chapter 4, building compact interferometers using coherent light. Setup 1 created fringes and real-time defect detection was performed, setup 2 was built and a sheared output was displayed, and setup 3 was mathematically evaluated (see Appendix B).

Future work includes taking relative measurements with compact interferometer setup 2 (Chapter 4.3). The system has been built to see that shearing can be formed, as shown in Figure 42, but the next steps are to create interference fringes and begin testing to see if relative measurements can be made with rough surfaces. Compact interferometer setup 3 (Chapter 4.4), depicted in Figure 43, needs to be built and tested to see if fringes can be formed in this configuration. All compact systems still require experimentation of both reflective and rough surfaces and their resolutions need to be quantified.

## REFERENCES

- [1] T. Nobukawa, T. Muroi, Y. Katano, N. Kinoshita, and N. Ishii, “Single-shot phase-shifting incoherent digital holography with multiplexed checkerboard phase gratings,” *Opt. Lett.*, vol. 43, no. 8, p. 1698, 2018.
- [2] K. Choi *et al.*, “Compact self-interference incoherent digital holographic camera system with real-time operation,” *Opt. Express*, vol. 27, no. 4, p. 4818, 2019.
- [3] K. Falaggis, T. Kozacki, and M. Kujawinska, “Computation of highly off-axis diffracted fields using the band-limited angular spectrum method with suppressed Gibbs related artifacts,” *Appl. Opt.*, vol. 52, no. 14, pp. 3288–3297, 2013.
- [4] T. Kozacki, K. Falaggis, and M. Kujawinska, “Computation of diffracted fields for the case of high numerical aperture using the angular spectrum method,” *Appl. Opt.*, vol. 51, no. 29, pp. 7080–7088, 2012.
- [5] B. Vohnsen, “A short history of optics,” *Phys. Scr. T*, vol. T109, pp. 75–79, 2004.
- [6] E. Hecht, *Optics*, 5th ed. Pearson Education, Incorporated, 2017.
- [7] G. Matteucci, R. Castaneda, S. Serna, F. Medina, and J. Garcia-Sucerquia, “Discovering the puzzling behaviour of electrons with the Grimaldi-Young experiment,” *Eur. J. Phys.*, vol. 31, no. 2, pp. 347–356, 2010.
- [8] A. V. Yurkin, “New view on the diffraction discovered by Grimaldi and Gaussian beams,” pp. 1–18, 2013.
- [9] P. Hariharan, *Basics of Interferometry*. Elsevier, 2010.
- [10] A. T. Forrester, “On Coherence Properties of Light Waves,” *Am. J. Phys.*, vol. 24, no. 4, pp. 192–196, 1956.
- [11] D. Attwood, “Spatial and Temporal Coherence at very short wavelengths.” UC Berkeley, 2016.
- [12] Y. Deng and D. Chu, “Coherence properties of different light sources and their effect on the image sharpness and speckle of holographic displays,” *Sci. Rep.*, vol. 7, no. 1, pp. 1–12, 2017.
- [13] T. W. Cronin and J. Marshall, “Patterns and properties of polarized light in air and water,” *Philos. Trans. R. Soc. B Biol. Sci.*, vol. 366, no. 1565, pp. 619–626, 2011.
- [14] M. Karakaya, “CHARACTERIZATION OF MOLECULAR BEAM EPITAXIALLY GROWN CDTE A Thesis Submitted to The Graduate School of Engineering and Sciences of İzmir Institute of Technology in Physics,” no. December 2014, 2016.

- [15] R. Porras-Aguilar, K. Falaggis, J. C. Ramirez-San-Juan, and R. Ramos-Garcia, "Self-calibrating common-path interferometry," *Opt. Express*, vol. 23, no. 3, p. 3327, 2015.
- [16] R. Porras-Aguilar, F. Hadavandmirzaee, D. Williams, and T. Suleski, "Arbitrary phase shifting in diffraction common path interferometry," no. August 2018, p. 31, 2018.
- [17] R. Schödel, A. Nicolaus, and G. Bönsch, "Phase-stepping interferometry: methods for reducing errors caused by camera nonlinearities," *Appl. Opt.*, vol. 41, no. 1, p. 55, 2002.
- [18] Y.-Y. Cheng and J. C. Wyant, "Two-wavelength phase shifting interferometry," *Appl. Opt.*, vol. 23, no. 24, p. 4539, 1984.
- [19] R. Leach, *Optical Measurement of Surface Topography*. Springer-Verlag Berlin Heidelberg, 2011.
- [20] L. A. DeMars, M. Miłkowska-Zdańkowska, K. Falaggis, and R. Porras-Aguilar, "Single-shot phase calibration of a spatial light modulator using geometric phase interferometry," *Appl. Opt.*, vol. 59, no. 13, p. D125, 2020.
- [21] K. Choi, J. Yim, and S.-W. Min, "Achromatic phase shifting self-interference incoherent digital holography using linear polarizer and geometric phase lens," *Opt. Express*, vol. 26, no. 13, p. 16212, 2018.
- [22] J. Rosen, B. Katz, and G. Brooker, "Review of three-dimensional holographic imaging by Fresnel incoherent correlation holograms," *3D Res.*, vol. 1, no. 1, pp. 28–35, 2010.
- [23] J. Rosen *et al.*, "Recent advances in self-interference incoherent digital holography," *Adv. Opt. Photonics*, vol. 11, no. 1, p. 1, 2019.
- [24] R. Kelner and J. Rosen, "Digital spatially incoherent fourier holography," *Front. Opt. FIO 2012*, vol. 32, no. 8, pp. 912–914, 2007.
- [25] E. N. Leith and J. Upatnieks, "Holography with Achromatic -Fringe Systems," *Opt. Soc. Am.*, vol. 57, no. 8, pp. 975–980, 1967.
- [26] S. Paul, I. S. Sevcenco, and P. Agathoklis, "Multi-exposure and multi-focus image fusion in gradient domain," *J. Circuits, Syst. Comput.*, vol. 25, no. 10, pp. 1–18, 2016.
- [27] I. S. Sevcenco, P. J. Hampton, and P. Agathoklis, "A wavelet based method for image reconstruction from gradient data with applications," *Multidimens. Syst. Signal Process.*, vol. 26, no. 3, pp. 717–737, 2015.
- [28] A. Greenbaum, W. Luo, B. Khademhosseini, T. W. Su, A. F. Coskun, and A.

Ozcan, "Increased space-bandwidth product in pixel super-resolved lensfree on-chip microscopy," *Sci. Rep.*, vol. 3, pp. 1–8, 2013.

- [29] J. L. Gresty, *Optical Shop Testing*, vol. 26, no. 7. 1979.
- [30] C. Elster and I. Weingärtner, "Solution to the shearing problem," *Appl. Opt.*, vol. 38, no. 23, p. 5024, 1999.
- [31] M. P. Rimmer and J. C. Wyant, "Evaluation of Large Aberrations Using a Lateral-Shear Interferometer Having Variable Shear," *Appl. Opt.*, vol. 14, no. 1, p. 142, 1975.
- [32] M. P. Rimmer, "Method for Evaluating Lateral Shearing Interferograms," *Appl. Opt.*, vol. 13, no. 3, p. 623, 1974.
- [33] A. Varghese, B. Das, and R. K. Singh, "Highly stable lens-less digital holography using cyclic lateral shearing interferometer and residual decollimated beam," *Opt. Commun.*, vol. 422, no. January, pp. 3–7, 2018.
- [34] B. Schaefer, E. Collett, R. Smyth, D. Barrett, and B. Fraher, "Measuring the Stokes polarization parameters," *Am. J. Phys.*, vol. 75, no. 2, pp. 163–168, 2007.
- [35] P. J. Wu and J. T. Walsh, "Stokes polarimetry imaging of rat tail tissue in a turbid medium: degree of linear polarization image maps using incident linearly polarized light," *J. Biomed. Opt.*, vol. 11, no. 1, p. 014031, 2006.
- [36] E. Sanchez, M. E. Benedet, D. P. Willemann, A. V. Fantin, and A. G. Albertazzi, "Analysis of a shearography device using a Wollaston prism and polarization phase shifting," *Interferom. XVIII*, vol. 9960, no. August 2016, p. 996015, 2016.

## APPENDIX A: VARIABLES USED IN MATHEMATICAL CALCULATIONS

Table A.1 gives a list of variables used in calculations and their meaning.

TABLE A.1 List of variables used in mathematical calculations.

CHAPTER 1: BACKGROUND	
$o$	object distance
$i$	image distance
$f$	focal length
$\lambda$	wavelength
$c$	speed of light
$\nu$	temporal frequency
$E$	electric field
$a$	amplitude
$k$	wave number
$\omega$	angular frequency
$t$	time
$\epsilon$	initial phase
$r$	position vector
$I_k$	intensity at angle $k$
$\phi$	phase
$L_c$	temporal coherence length
$J$	Jones vector
CHAPTER 2: EXPERIMENTAL SETUP AND PROCEDURE – GP LENS	
$I_1$	intensity from polarized camera sensor at 0 degrees

$I_2$	intensity from polarized camera sensor at 45 degrees
$I_3$	intensity from polarized camera sensor at 90 degrees
$I_4$	intensity from polarized camera sensor at 135 degrees
$E'$	output electric field after transmission
$\Omega$	arbitrary angle of polarization of linear polarizer
UH	complex wavefield
$z_o$	object distance
$z_{obj-gp}$	distance between the objective and GP lens
$z_{gp-rl}$	distance between the GP and relay lens, or primary principal plane
$z_h$	distance between the relay lens, or secondary principal plane, and the camera sensor
$d_{gp}^{\pm}$	GP lens imaging distances
$d_{rl}^{\pm}$	relay lens imaging distances
$z_{rec}$	reconstruction distance of GP lens setup
U	wavefield after using AS method
$U_0$	initial two-dimensional complex wavefield
g	phase term
$f_{x,y,z}$	spatial frequency

## APPENDIX B: WIGNER ANALYSES FOR EXPERIMENTAL SETUPS

Wigner analyses were performed in Mathematica® before each setup was built, and this allows the evaluation of how the light propagates through the system as it propagates through each optical component. The results give properties such as magnification, distortion, defocusing, or offsets when the light goes through the setup.

### 1. GP Lens Setup

```
In[1]:= f[x_, v_] = W[x, v];
```

```
f2[x_, v_, zO_] = f[x-lam*zO*v, v];
```

```
f3[x_, v_, zO_, fO_] = f2[x, v+x/(lam*fO), zO];
```

```
f4[x_, v_, zO_, fO_, zOGP_] = f3[x-lam*zOGP*v, v, zO, fO];
```

```
f5[x_, v_, zO_, fO_, zOGP_, fGP_] = f4[x, v+x/lam/fGP, zO, fO, zOGP];
```

```
f6[x_, v_, zO_, fO_, zOGP_, fGP_, zRL_] = f5[x-lam*zRL*v, v, zO, fO, zOGP, fGP];
```

```
f7[x_, v_, zO_, fO_, zOGP_, fGP_, zRL_, fRL_] = f6[x, v+x/lam/fRL, zO, fO, zOGP, fGP, zRL];
```

```
f8[x_, v_, zO_, fO_, zOGP_, fGP_, zRL_, fRL_, zCAM_] = f7[x-lam*zCAM*v, v, zO, fO, zOGP, fGP, zRL, fRL];
```

(\* the function f is the Wigner function of the object and the function f8 is the Wigner result of the object at the camera sensor after passing through the imaging system \*)

(\* Here we simply use variables, and make the calculation twice, once with +fGP and once with -fGP \*)

```
f8[x, v, zO, fO, zOGP, fGP, zRL, fRL, zCAM] //FullSimplify//Expand//FullSimplify
```

```
f8[x, v, zO, fO, zOGP, -fGP, zRL, fRL, zCAM] //FullSimplify//Expand//FullSimplify
```

(\* This is the result from above. A Wigner function in form of "  $W(Mx, v/M + d(\phi)/dx * 1/(2\pi))$  " Gives information about the magnification M and the phase induced by the imaging system\*)

```
Out[9]= W[(1/(fGP fO fRL))(-(-zO zOGP+fO (zO+zOGP)) (-x zRL+lam v zCAM zRL+fRL (x-lam v (zCAM+zRL)))+fGP (-fRL x zO+(x-lam v zCAM) zO
```

$$\begin{aligned} & (zOGP+zRL)+fRL \text{ lam } v \text{ zO } (zCAM+zOGP+zRL)-fO (x-\text{lam } v \text{ zCAM}) \\ & (zO+zOGP+zRL)+fO \text{ fRL } (x-\text{lam } v \text{ (zCAM+zO+zOGP+zRL)})), (1/(fGP \text{ fO } fRL \\ & \text{lam}))((fO-zOGP) (-x \text{ zRL+lam } v \text{ zCAM } zRL+fRL (x-\text{lam } v \text{ (zCAM+zRL)})))+fGP (fO \\ & (x+\text{lam } v \text{ (fRL-zCAM)})-(x-\text{lam } v \text{ zCAM}) (zOGP+zRL)+fRL (x-\text{lam } v \\ & (zCAM+zOGP+zRL))))] \end{aligned}$$

$$\begin{aligned} \text{Out}[10]= & W[(1/(fGP \text{ fO } fRL))((-zO \text{ zOGP+fO } (zO+zOGP)) (-x \text{ zRL+lam } v \text{ zCAM} \\ & zRL+fRL (x-\text{lam } v \text{ (zCAM+zRL)})))+fGP (-fRL \text{ x } zO+(x-\text{lam } v \text{ zCAM}) zO \\ & (zOGP+zRL)+fRL \text{ lam } v \text{ zO } (zCAM+zOGP+zRL)-fO (x-\text{lam } v \text{ zCAM}) \\ & (zO+zOGP+zRL)+fO \text{ fRL } (x-\text{lam } v \text{ (zCAM+zO+zOGP+zRL)})), (1/(fGP \text{ fO } fRL \text{ lam}))(- \\ & (fO-zOGP) (-x \text{ zRL+lam } v \text{ zCAM } zRL+fRL (x-\text{lam } v \text{ (zCAM+zRL)})))+fGP (fO (x+\text{lam } v \\ & (fRL-zCAM))-(x-\text{lam } v \text{ zCAM}) (zOGP+zRL)+fRL (x-\text{lam } v \text{ (zCAM+zOGP+zRL)}))] \end{aligned}$$

$$\text{In}[11]:= \text{FREQplus}[x\_ , v\_ , zO\_ , fO\_ , zOGP\_ , fGP\_ , zRL\_ , fRL\_ , zCAM\_ ]=$$

$$\begin{aligned} & ((fO-zOGP) (-x \text{ zRL+lam } v \text{ zCAM } zRL+fRL (x-\text{lam } v \text{ (zCAM+zRL)})))+fGP (fO (x+\text{lam } \\ & v \text{ (fRL-zCAM)})-(x-\text{lam } v \text{ zCAM}) (zOGP+zRL)+fRL (x-\text{lam } v \\ & (zCAM+zOGP+zRL)))/(fGP \text{ fO } fRL \text{ lam}); \end{aligned}$$

$$\text{FREQminus}[x\_ , v\_ , zO\_ , fO\_ , zOGP\_ , fGP\_ , zRL\_ , fRL\_ , zCAM\_ ]=$$

$$\begin{aligned} & (-(fO-zOGP) (-x \text{ zRL+lam } v \text{ zCAM } zRL+fRL (x-\text{lam } v \text{ (zCAM+zRL)})))+fGP (fO (x+\text{lam } \\ & v \text{ (fRL-zCAM)})-(x-\text{lam } v \text{ zCAM}) (zOGP+zRL)+fRL (x-\text{lam } v \\ & (zCAM+zOGP+zRL)))/(fGP \text{ fO } fRL \text{ lam}); \end{aligned}$$

$$\text{Collect}[\text{FREQplus}[x, v, zO, fO, zOGP, fGP, zRL, fRL, zCAM]-\text{FREQminus}[x, v, zO, fO, zOGP, fGP, zRL, fRL, zCAM], x, v]$$

$$\text{FREQplus}[x, v, zO, fO, zOGP, fGP, zRL, fRL, zCAM]-\text{FREQminus}[x, v, zO, fO, zOGP, fGP, zRL, fRL, zCAM]//\text{FullSimplify}//\text{Expand}//\text{FullSimplify}$$

(\* the difference is proportional to (fO-zOGP). So if the GP lens is placed in the focal plane of the objective lens, both beams will have the same phase\*)

$$\begin{aligned} \text{Out}[13]= & x \text{ v}[(fO-zOGP)/(fGP \text{ fO } \text{lam})-(-fO+zOGP)/(fGP \text{ fO } \text{lam})-((fO-zOGP) \\ & zRL)/(fGP \text{ fO } fRL \text{ lam})+((-fO+zOGP) zRL)/(fGP \text{ fO } fRL \text{ lam})]+v[(v \text{ zCAM } (fO-zOGP) \\ & zRL)/(fGP \text{ fO } fRL)-(v \text{ zCAM } (-fO+zOGP) zRL)/(fGP \text{ fO } fRL)-(v (fO-zOGP) \\ & (zCAM+zRL))/(fGP \text{ fO})+(v (-fO+zOGP) (zCAM+zRL))/(fGP \text{ fO})] \end{aligned}$$

$$\text{Out}[14]= (2 (fO-zOGP) (-x \text{ zRL+lam } v \text{ zCAM } zRL+fRL (x-\text{lam } v \text{ (zCAM+zRL)})))/(fGP \text{ fO } fRL \text{ lam})$$

$$\text{In}[15]:= (*\text{setting } fO = zOGP*)$$

$$f8[x, v, zO, fO, fO, fGP, zRL, fRL, zCAM] //\text{FullSimplify}//\text{Expand}//\text{FullSimplify}$$

$$f8[x, v, zO, fO, fO, -fGP, zRL, fRL, zCAM] //\text{FullSimplify}//\text{Expand}//\text{FullSimplify}$$

Out[15]=  $W[x+(1/(fO \text{ fRL}))(-fO (fO (x+lam \text{ v} (fRL-zCAM))+fRL \text{ lam} \text{ v} \text{ zCAM})+fRL (-x+lam \text{ v} \text{ zCAM}) \text{ zO}-(x+lam \text{ v} (fRL-zCAM)) (fO-zO) \text{ zRL})+(fO (-fRL \text{ x}+(x-lam \text{ v} \text{ zCAM}) \text{ zRL}+fRL \text{ lam} \text{ v} (zCAM+zRL)))/(fGP \text{ fRL}),(-x \text{ zRL}+lam \text{ v} \text{ zCAM} \text{ zRL}+fRL (x-lam \text{ v} (zCAM+zRL)))/(fO \text{ fRL} \text{ lam})]$

Out[16]=  $W[x+(1/(fO \text{ fRL}))(-fO (fO (x+lam \text{ v} (fRL-zCAM))+fRL \text{ lam} \text{ v} \text{ zCAM})+fRL (-x+lam \text{ v} \text{ zCAM}) \text{ zO}-(x+lam \text{ v} (fRL-zCAM)) (fO-zO) \text{ zRL})+(fO (-x \text{ zRL}+lam \text{ v} \text{ zCAM} \text{ zRL}+fRL (x-lam \text{ v} (zCAM+zRL)))/(fGP \text{ fRL}),(-x \text{ zRL}+lam \text{ v} \text{ zCAM} \text{ zRL}+fRL (x-lam \text{ v} (zCAM+zRL)))/(fO \text{ fRL} \text{ lam})]$

In[17]:= (\*difference in horizontal shear\*)

SPATIALplus[x\_, v\_, zO\_, fO\_, zOGP\_, fGP\_, zRL\_, fRL\_, zCAM\_]=

$(-fO (fO (x+lam \text{ v} (fRL-zCAM))+fRL \text{ lam} \text{ v} \text{ zCAM})+fRL (-x+lam \text{ v} \text{ zCAM}) \text{ zO}-(x+lam \text{ v} (fRL-zCAM)) (fO-zO) \text{ zRL})/(fO \text{ fRL})+(fO (-fRL \text{ x}+(x-lam \text{ v} \text{ zCAM}) \text{ zRL}+fRL \text{ lam} \text{ v} (zCAM+zRL)))/(fGP \text{ fRL});$

SPATIALminus[x\_, v\_, zO\_, fO\_, zOGP\_, fGP\_, zRL\_, fRL\_, zCAM\_]=

$(-fO (fO (x+lam \text{ v} (fRL-zCAM))+fRL \text{ lam} \text{ v} \text{ zCAM})+fRL (-x+lam \text{ v} \text{ zCAM}) \text{ zO}-(x+lam \text{ v} (fRL-zCAM)) (fO-zO) \text{ zRL})/(fO \text{ fRL})+(fO (-x \text{ zRL}+lam \text{ v} \text{ zCAM} \text{ zRL}+fRL (x-lam \text{ v} (zCAM+zRL)))/(fGP \text{ fRL});$

SPATIALplus[x, v, zO, fO, zOGP, fGP, zRL, fRL, zCAM] - SPATIALminus[x, v, zO, fO, zOGP, fGP, zRL, fRL, zCAM]//FullSimplify//Expand

Collect[SPATIALplus[x, v, zO, fO, zOGP, fGP, zRL, fRL, zCAM], v]

Collect[SPATIALminus[x, v, zO, fO, zOGP, fGP, zRL, fRL, zCAM], x,v]

(\*and also the difference for completeness \*)

Collect[SPATIALplus[x, v, zO, fO, zOGP, fGP, zRL, fRL, zCAM] - SPATIALminus[x, v, zO, fO, zOGP, fGP, zRL, fRL, zCAM], x,v]

Out[19]=  $-((2 \text{ fO} \text{ x})/fGP)+(2 \text{ fO} \text{ lam} \text{ v} \text{ zCAM})/fGP+(2 \text{ fO} \text{ lam} \text{ v} \text{ zRL})/fGP+(2 \text{ fO} \text{ x} \text{ zRL})/(fGP \text{ fRL})-(2 \text{ fO} \text{ lam} \text{ v} \text{ zCAM} \text{ zRL})/(fGP \text{ fRL})$

Out[20]=  $-((fO \text{ x})/fGP)-(fO \text{ x})/fRL-(x \text{ zO})/fO+(fO \text{ x} \text{ zRL})/(fGP \text{ fRL})-(x (fO-zO) \text{ zRL})/(fO \text{ fRL})+v (-((fO \text{ lam} (fRL-zCAM))/fRL)-lam \text{ zCAM}+(lam \text{ zCAM} \text{ zO})/fO-(fO \text{ lam} \text{ zCAM} \text{ zRL})/(fGP \text{ fRL})-(lam (fRL-zCAM) (fO-zO) \text{ zRL})/(fO \text{ fRL})+(fO \text{ lam} (zCAM+zRL))/fGP)$

Out[21]=  $x \text{ v}[fO/fGP-fO/fRL-zO/fO-(fO \text{ zRL})/(fGP \text{ fRL})-((fO-zO) \text{ zRL})/(fO \text{ fRL})]+v[-((fO \text{ lam} \text{ v} (fRL-zCAM))/fRL)-lam \text{ v} \text{ zCAM}+(lam \text{ v} \text{ zCAM} \text{ zO})/fO+(fO \text{ lam} \text{ v} \text{ zCAM} \text{ zRL})/(fGP \text{ fRL})-(lam \text{ v} (fRL-zCAM) (fO-zO) \text{ zRL})/(fO \text{ fRL})-(fO \text{ lam} \text{ v} (zCAM+zRL))/fGP]$

Out[22]= x v[-((2 fO)/fGP)+(2 fO zRL)/(fGP fRL)]+v[-((2 fO lam v zCAM zRL)/(fGP fRL))+2 fO lam v (zCAM+zRL)/fGP]

In[23]:= Collect[SPATIALplus[x, v, zO, fO, zOGP, fGP, zRL, fRL, fRL], x,v]

Collect[SPATIALminus[x, v, zO, fO, zOGP, fGP, zRL, fRL, fRL], x,v]

Out[23]= x v[-(fO/fGP)-fO/fRL-zO/fO+(fO zRL)/(fGP fRL)-((fO-zO) zRL)/(fO fRL)]+v[-fRL lam v+(fRL lam v zO)/fO-(fO lam v zRL)/fGP+(fO lam v (fRL+zRL))/fGP]

Out[24]= x v[fO/fGP-fO/fRL-zO/fO-(fO zRL)/(fGP fRL)-((fO-zO) zRL)/(fO fRL)]+v[-fRL lam v+(fRL lam v zO)/fO+(fO lam v zRL)/fGP-(fO lam v (fRL+zRL))/fGP]

In[25]:= Collect[(-x zRL+lam v zCAM zRL+fRL (x-lam v (zCAM+zRL)))/(fO fRL lam), x, v]

Out[25]= x v[(fRL-zRL)/(fO fRL lam)]+v[(lam v zCAM zRL-fRL lam v (zCAM+zRL))/(fO fRL lam)]

In[26]:= x v[(fRL-zRL)/(fO fRL lam)]+v[(lam v zCAM zRL-fRL lam v (zCAM+zRL))/(fO fRL lam)]

SPATIALplus[x, v, zO, fO, zOGP, fGP, zRL, fRL, zCAM] - SPATIALminus[x, v, zO, fO, zOGP, fGP, zRL, fRL, zCAM]//FullSimplify//Expand

Out[26]= x v[(fRL-zRL)/(fO fRL lam)]+v[(lam v zCAM zRL-fRL lam v (zCAM+zRL))/(fO fRL lam)]

Out[27]= -((2 fO x)/fGP)+(2 fO lam v zCAM)/fGP+(2 fO lam v zRL)/fGP+(2 fO x zRL)/(fGP fRL)-(2 fO lam v zCAM zRL)/(fGP fRL)

In[28]:= FREQplus[x, v, zO, fO, fO, fGP, fRL, fRL, zCAM]//Expand

FREQminus[x, v, zO, fO, fO, fGP, fRL, fRL, zCAM]//Expand

Out[28]= -((fRL v)/fO)

Out[29]= -((fRL v)/fO)

In[30]:= f8[x, v, zO, fO, fO, fGP, fRL, fRL, zCAM] //FullSimplify//Expand

f8[x, v, zO, fO, fO, -fGP, fRL, fRL, zCAM] //FullSimplify//Expand

Out[30]= W[-fRL lam v-(fO x)/fRL+fO lam v (-1+fRL/fGP+zCAM/fRL)+(fRL lam v zO)/fO,-((fRL v)/fO)]

Out[31]= W[-fRL lam v-(fO fRL lam v)/fGP-(fO (x+lam v (fRL-zCAM)))/fRL+(fRL lam v zO)/fO,-((fRL v)/fO)]

In[32]:= Collect[fRL lam v-(fO x)/fRL+fO lam v (-1+fRL/fGP+zCAM/fRL)+(fRL lam v zO)/fO, v\*lam]

Collect[-fRL lam v-(fO fRL lam v)/fGP-(fO (x+lam v (fRL-zCAM)))/fRL+(fRL lam v zO)/fO, v\*lam]

Out[32]= -((fO x)/fRL)+lam v (fRL+fO (-1+fRL/fGP+zCAM/fRL)+(fRL zO)/fO)

Out[33]= -((fO x)/fRL)+lam v (-fRL-(fO fRL)/fGP-(fO (fRL-zCAM))/fRL+(fRL zO)/fO)

## 2. GP grating Setup

In[1]:=  $W[x\_ , v\_ ] = \{x, v\};$

$f[x\_ , v\_ ] = W[x, v];$

(\*propagation through space\*)

$f2[x\_ , v\_ , zO\_ ] = f[x-lam*zO*v, v];$

(\*propagate through grating\*)

$f3[x\_ , v\_ , zO\_ , vG\_ ] = f2[x, v+vG, zO];$

(\*propagate through space\*)

$f4[x\_ , v\_ , zO\_ , vG\_ , z1\_ ] = f3[x-lam*z1*v, v, zO, vG];$

(\*propagate through lens\*)

$f5[x\_ , v\_ , zO\_ , vG\_ , z1\_ , fO1\_ ] = f4[x, v+x/lam/fO1, zO, vG, z1];$

(\*propagate through space\*)

$f6[x\_ , v\_ , zO\_ , vG\_ , z1\_ , fO1\_ , z2\_ ] = f5[x-lam*z2*v, v, zO, vG, z1, fO1];$

(\*propagate through lens\*)

$f7[x\_ , v\_ , zO\_ , vG\_ , z1\_ , fO1\_ , z2\_ , fO2\_ ] = f6[x, v+x/lam/fO2, zO, vG, z1, fO1, z2];$

(\*propagate through space\*)

$f8[x\_ , v\_ , zO\_ , vG\_ , z1\_ , fO1\_ , z2\_ , fO2\_ , z3\_ ] = f7[x-lam*z3*v, v, zO, vG, z1, fO1, z2, fO2];$

(\*propagate through grating\*)

$f9[x\_ , v\_ , zO\_ , vG\_ , z1\_ , fO1\_ , z2\_ , fO2\_ , z3\_ , vG2\_ ] = f8[x, v+vG2, zO, vG, z1, fO1, z2, fO2, z3];$

(\*propagate through space\*)

$f10[x\_ , v\_ , zO\_ , vG\_ , z1\_ , fO1\_ , z2\_ , fO2\_ , z3\_ , vG2\_ , z4\_ ] = f9[x-lam*z4*v, v, zO, vG, z1, fO1, z2, fO2, z3, vG2];$

(\*propagate through relay lens\*)

$f11[x\_ , v\_ , zO\_ , vG\_ , z1\_ , fO1\_ , z2\_ , fO2\_ , z3\_ , vG2\_ , z4\_ , fO3\_ ] = f10[x, v+x/lam/fO3, zO, vG, z1, fO1, z2, fO2, z3, vG2, z4];$

(\*propagate through space\*)

```
f12[x_, v_, zO_, vG_, z1_, fO1_, z2_, fO2_, z3_, vG2_, z4_, fO3_, zCAM_] = f11[x - lam * zCAM * v, v, zO, vG, z1, fO1, z2, fO2, z3, vG2, z4, fO3];
```

```
f12[x, v, zO, vG, fO1, fO1, fO1, fO1, fO1, vG, fO3, fO3, zCAM] // FullSimplify // Expand // FullSimplify
```

```
Out[14] = {lam v zO + ((x - lam v zCAM) zO) / fO3 + (fO3 lam v (fO1 + zO)) / fO1, -(x / (fO3 lam)) + v (-1 - fO3 / fO1 + zCAM / fO3)}
```

In[15]:= (\*reconstruction z distance to sharp image\*)

```
f13[x_, v_, zO_, vG_, z1_, fO1_, z2_, fO2_, z3_, vG2_, z4_, fO3_, zCAM_, zrec_] =
```

```
f12[x - lam * zrec * v, v, zO, vG, z1, fO1, z2, fO2, z3, vG2, z4, fO3, zCAM];
```

```
f13[x, v, zO, vG, fO1, fO1, fO1, fO1, fO1, vG, fO3, fO3, zCAM, - zCAM + (fO3 * (fO1 + fO3)) / fO1] // FullSimplify // Expand // FullSimplify
```

```
Out[16] = {fO3 lam v + (x zO) / fO3, -(x / (fO3 lam))}
```

### 3. Compact Interferometer Setups

#### 3.1 Setup 1

In[17]:= W[x\_, v\_] = {x, v};

f[x\_, v\_] = W[x, v];

(\*propagate through space\*)

f2[x\_, v\_, zO\_] = f[x-lam\*zO\*v, v];

(\*propagate through grating\*)

f3[x\_, v\_, zO\_, vG\_] = f2[x, v+vG, zO];

(\*propagate through space\*)

f4[x\_, v\_, zO\_, vG\_, z1\_] = f3[x-lam\*z1\*v, v, zO, vG];

(\*propagate through lens\*)

f5[x\_, v\_, zO\_, vG\_, z1\_, fO1\_] = f4[x, v+x/lam/fO1, zO, vG, z1];

(\*propagate through space to object\*)

f6[x\_, v\_, zO\_, vG\_, z1\_, fO1\_, z2\_] = f5[x-lam\*z2\*v, v, zO, vG, z1, fO1];

(\*propagation through space from object\*)

f7[x\_, v\_, zO\_, vG\_, z1\_, fO1\_, z2\_, z3\_] = f6[x-lam\*z3\*v, v, zO, vG, z1, fO1, z2];

(\*propagate through lens\*)

f8[x\_, v\_, zO\_, vG\_, z1\_, fO1\_, z2\_, z3\_, fO2\_] = f7[x, v+x/lam/fO2, zO, vG, z1, fO1, z2, z3];

(\*propagate through space\*)

f9[x\_, v\_, zO\_, vG\_, z1\_, fO1\_, z2\_, z3\_, fO2\_, z4\_] = f8[x-lam\*z4\*v, v, zO, vG, z1, fO1, z2, z3, fO2];

(\*propagate through grating\*)

f10[x\_, v\_, zO\_, vG\_, z1\_, fO1\_, z2\_, z3\_, fO2\_, z4\_, vG2\_] =

f9[x, v+vG2, zO, vG, z1, fO1, z2, z3, fO2, z4];

(\*propagate through space\*)

```

f11[x_, v_, zO_, vG_, z1_, fO1_, z2_, z3_, fO2_, z4_, vG2_, z5_] =
    f10[x-lam*z5*v, v, zO, vG, z1, fO1, z2, z3, fO2, z4, vG2];
(*propagate through lens*)
f12[x_, v_, zO_, vG_, z1_, fO1_, z2_, z3_, fO2_, z4_, vG2_, z5_, fO3_] =
    f11[x, v+x/lam/fO3, zO, vG, z1, fO1, z2, z3, fO2, z4, vG2, z5];
(*propagate through space*)
f13[x_, v_, zO_, vG_, z1_, fO1_, z2_, z3_, fO2_, z4_, vG2_, z5_, fO3_, z6_] =
    f12[x-lam*z6*v, v, zO, vG, z1, fO1, z2, z3, fO2, z4, vG2, z5, fO3];
f13[x, v, z, vG, F-z, F, F+D, F+D, F, F+q, vG, -q+Z+r, F, -
r+Zcam]//FullSimplify//Expand//FullSimplify
Out[31]= {(x (-F+r+Z)+lam (F vG (q-z)+v (r+Z) (r-Zcam)+F v (Z+Zcam)))/F,(1/(F^3
lam))(-F^3 lam v-F^2 (x+lam v (r-Zcam))+2 D (r+Z) (x+lam v (r-Zcam))+2 D F (lam q
vG-x+lam v (Z+Zcam)))}
In[32]:= (* now adjust the position of the last lens to compensate the x-term by adjusting
r term*)
Solve[(x (-F+r+Z))/F==0, r]//FullSimplify//Expand//FullSimplify
(* move now the last lens to by the distance r = F-Z *)
f13[x, v, z, vG, F-z, F, F+D, F+D, F, F+q, vG, -q+Z+(F-Z), F, -(F-
Z)+Zcam]//FullSimplify//Expand//FullSimplify
Out[32]= {{r->F-Z}}
Out[33]= {lam (F v+vG (q-z)),(2 D lam (F v+q vG)-F x+F lam v (-2 F+Z+Zcam))/(F^2
lam)}
In[34]:= f13[x, v, 0,0 , 0, Infinity, 0, F+D, F, F+q, vG, -q+F, F,
Zcam2]//FullSimplify//Expand//FullSimplify
Out[34]= {-F lam (v+vG)+D lam (v+(q vG)/F)-x+lam v Zcam2,-((F v+q vG)/F)}
In[35]:= (* bring the object now into focus (no lam*v term in the spatial domain)*)
Solve[-F lam (v)+D lam (v)+lam v * Zcam2 == 0,
Zcam2]//FullSimplify//Expand//FullSimplify
Out[35]= {{Zcam2->-D+F}}

```

In[36]:= (\* Zcam can be adjusted, by moving the camera so that the object is always in focus\*)

f13[x, v, 0, 0, 0, Infinity, 0, F+D, F, F+q, vG, -q+F, F, F-D]//FullSimplify//Expand//FullSimplify

Out[36]=  $\{-F \lambda vG + (D \lambda q vG)/F - x, -((F v + q vG)/F)\}$

In[37]:= (\* Now Let's consider again the whole system \[Rule] Fourier transform of the Source, because of three (2f)-systems \*)

f13[x, v, z, vG, F-z+s, F, F+D, F+D, F, F+q, vG, -q+F, F, F-D]//FullSimplify//Expand//FullSimplify

Out[37]=  $\{F \lambda v - (2 D \lambda q s vG)/F^2 + (s (-D \lambda v + x))/F + \lambda vG (q + s - z), (D F \lambda v + 2 D \lambda q vG - F x)/(F^2 \lambda)\}$

In[38]:= (\* The previous results show that q produces a chirp. We need to align the grating to achieve  $q = 0$  \*)

f13[x, v, z, vG, F-z, F, F+D, F+D, F, F, vG, +F, F, F-D]//FullSimplify//Expand//FullSimplify//Expand

Out[38]=  $\{F \lambda v - \lambda vG z, (D v)/F - x/(F \lambda)\}$

In[39]:= (\* This shows, by adjusting the first grating, we can adjust the shear\*)

f13[x, v, z, vG, F-z+s, F, F+D, F+D, F, F-q, vG, +F+q, F, F-D] -

f13[x, v, z, -vG, F-z+s, F, F+D, F+D, F, F-q, -vG, +F+q, F, F-D]//FullSimplify//Expand//FullSimplify//Expand

Out[39]=  $\{-2 \lambda q vG + 2 \lambda s vG + (4 D \lambda q s vG)/F^2 - 2 \lambda vG z, -((4 D q vG)/F^2)\}$

In[40]:= f13[x, v, 0, 0, 0, Infinity, 0, F+D, F, F, vG, +F, F, F-D]-

f13[x, v, 0, 0, 0, Infinity, 0, F+D, F, F, -vG, +F, F, F-D]//FullSimplify//Expand//FullSimplify//Expand

Out[40]=  $\{-2 F \lambda vG, 0\}$

In[41]:= (\* Conclusions\*)

(\* all three lenses must have the same focal length, q needs to be 0, z can adjust the shear, and adjusting Zcam2 brings the object in focus. \*)

## 3.2 Setups 2 and 3

```

In[42]:= W[x_, v_] = {x,v};

f[x_, v_] = W[x, v];

f2[x_, v_, zO_] = f[x-lam*zO*v, v]; (*propagation through space*)

f3[x_, v_, zO_, fOb_] = f2[x, v+x/lam/fOb, zO]; (*propagate through objective*)

f4[x_, v_, zO_, fOb_, z1_] = f3[x-lam*z1*v, v, zO, fOb]; (*propagate through space*)

f5[x_, v_, zO_, fOb_, z1_, vG_] = f4[x, v+vG, zO, fOb, z1]; (*propagate through grating*)

f6[x_, v_, zO_, fOb_, z1_, vG_, z2_] = f5[x-lam*z2*v, v, zO, fOb, z1, vG]; (*propagate
through space*)

f7[x_, v_, zO_, fOb_, z1_, vG_, z2_, zeff_] = f6[x-lam*zeff*v, v, zO, fOb, z1, vG, z2]
;(*propagate through space*)

f7[x, v, zO, fOb, z1, vG, z2, zeff] //FullSimplify//Expand//FullSimplify

Out[44]= {x+((-x+lam vG z1+lam v (z1+z2+zeff)) zO)/fOb-lam (vG (z1+zO)+v
(z1+z2+zeff+zO)),v+vG+x/(fOb lam)-(vG z1+v (z1+z2+zeff))/fOb}

In[45]:= f7[x, v, zO, fOb, 1/((1/fOb)-(1/zO)), vG, z2, -z2]
//FullSimplify//Expand//FullSimplify

Out[45]= {x-(x zO)/fOb,x/(fOb lam)+(fOb (v+vG))/(fOb-zO)}

In[46]:= (*solved for z1 to cancel out spatial domain*)

f7[x, v, zO, fOb, (zO*fOb)/(zO-fOb), vG, z2, 0] - f7[x, v, zO, fOb, (zO*fOb)/(zO-fOb), -
vG, z2, 0] //FullSimplify//Expand//FullSimplify

Out[46]= {0,(2 fOb vG)/(fOb-zO)}

```